3D-Printed Artificial Dielectrics for Beam Steering Metasurfaces

By

Touseef Hayat

A thesis submitted to Macquarie University

for the degree of Master of Research

School of Engineering

September 2018

Except where acknowledged in the customary manner, the material presented in this thesis is, to the best of my knowledge, original and has not been submitted in whole or part for a degree in any university.

Touseef Hayat

Acknowledgements

First and above all, I thank the Almighty who has given me the opportunity and granted me the capability to successfully complete the MRes degree. The dissertation appears in its current form due to the assistance and guidance of several people. I would therefore like to offer my sincere thanks to all of them.

I would like to express my sincere gratitude to my supervisor, Professor Karu Esselle, director of the Centre for Collaboration in Electromagnetic and Antenna Engineering (CELANE), who supported me throughout this project. I am extremely indebted to Dr. Usman Afzal for his invaluable guidance and continuous encouragement throughout my research work. I would like to convey my deepest gratitude and thanks to him.

I would also like to thank Dr Keith Imrie for his proofreading and valuable feedback in improving the quality of this thesis. I am also thankful to the admirable staff at the School of Engineering for their wonderful support. I wish to acknowledge Macquarie University for awarding me an international Research Training Pathway Scholarship (iRTP) and providing financial support. I also sincerely thank my parents, and my family as a whole, for their love and support throughout this project and my life. Last but not least, thanks to my friends for making me feel special, and being there when I needed them.

List of Publications

- **Touseef Hayat**, Karu Esselle, Muhammad Usman Afzal, Khushboo Singh "3D Printed All Dielectric Phase Correcting Surface for Resonant Cavity Antenna" In Antennas and Propagation (APCAP), 2018 IEEE 7th Asia-Pacific Conference.

Abstract

Fused decomposition 3D printing technology can be used to develop artificial dielectric meta-atoms that are not available commercially, with the advantage of low cost and little human intervention. A two-dimensional periodic arrangement of artificial dielectric meta-atoms forms a metasurface, which can serve as a platform to realize subwavelength-thick phase shifting (PS) structures. Such metasurfaces manipulate radio frequency (RF) waves and possess the ability to control the amplitude, phase and polarization of the field. The objective of this thesis is to develop highly transmitting sub-wavelength sized 3D printable meta-atoms that can inculcate a full 2π phase shift in the transmitting field. These meta-atoms are then used to design transmitting beam-steering metasurfaces. The meta-atom configuration developed uses one dielectric and two metallic layers. The dielectric permittivity and height are varied to achieve a full range of $[0, 2\pi]$ while ensuring transmission levels remain greater than -0.75 dB. Moreover, meta-atoms are used to design beam steering surfaces for resonant cavity antennas (RCA) operating at 20 GHz. A peak gain of 21.65 dBi was achieved and the RCA pattern can be steered to any elevation angle between 0° and 35° with less than 2dB gain variation.

Contents

List of Figures

List of Tables

Chapter 1

Introduction

Control and manipulation of optical and electromagnetic (EM) response originating from different sources, for instance LEDs (light emitting diodes), bandgap semiconductors, lasers and antennas has been a topic of considerable interest [1], [2]. Radiation response can be altered by perturbation of phase, amplitude or polarization of a field. Components with the ability to modify a propagating beam can be used for various communication and sensing applications. Traditional devices are based on concepts of wave absorption, refraction, reflection and diffraction. Manipulation is attained by propagating radiations through media of known refractive indices, which can be engineered to control the resultant beam. Due to rapid technological advances and increasing demand for miniaturized integrating tools, customary devices cannot be adapted for modern EM systems. Subsequently, the components comprising synthetic materials which are not readily available in nature are in great demand.

In recent years, customized metasurfaces have been used as phase shifters for various holographic applications [3]–[5]. One of the most interesting features of metasurfaces is to transform a given wavefront into the desired pattern, the objective being to achieve particular a beam shape in the far-field. These surfaces can be made to deflect the EM field in the desired direction by introducing appropriate phase shifts. Phase shifting metasurfaces are typically engineered to have uniform or non-uniform printed surfaces. However, it is also possible to develop such surfaces using artificial dielectric materials [6]. These artificial dielectric-based metasurfaces find applications in EM lenses, EM wave absorbers, phase shifters and antenna beam shaping. In comparison with printed metasurfaces, they are superior to conventional dielectrics in terms of possessing physical and fabricational supremacy.

In modern applications, we require dielectric materials that may not be commercially available. 3D printing techniques can be used to overcome limitations related to the dielectric constant and height of material. Non-complex meta-atom/unit cell configuration closer to a natural material with the ability to mimic the local response of natural dielectric can be fabricated using this printing facility. Printed unit cells spatially arranged on the basis of phased array theory can mimic the local response of a natural materials and be used effectively for beam steering. This can be achieved by keeping the structure lightweight, simple and small in size. The objective of this thesis is to explain the use of low loss 3D printable artificial dielectric materials for making metasurfaces.

1.1 Research Motivation

Metasurfaces comprise periodic structures with the ability to electrically or magnetically couple with the incident EM field. These nano-structured artificial components have generated great interest in recent years and produced remarkable results in the microwave regime. However, strong dispersion, high loss and restrictions related to commercially available materials have limited their practical applications. Not only that, the fabrication of micro- and nano-scale 3D structures has been cumbersome because it involves tedious machining and bonding steps which in turn escalates the component cost. 3D printing is a rapidly growing, low-cost, speedy and highly accurate process that has resulted in applications in manufacturing, industry and other fields of science. It offers more freedom and better accuracy than traditional machining methods. Moreover, because bonding and machining are not involved, this fabrication method adds to the physical robustness of the materials. Based on current trends, it has been observed that 3D printing is becoming more easily accessible and affordable with the passage of time. It is speculated that the cost of such designs will decrease even more in the future. 3D printing technology is tipped to become a billion-dollar market in the following decade because demand for it is increasing in the automotive and manufacturing industries.

1.2 Research Framework and Objectives

The research presented in this thesis has been conducted over a period of nine months beginning in November 2017, for partial fulfilment of the requirements for the degree of Master of Research (MRes) at Macquarie University. The research was funded by an international Research Training Pathway (iRTP) scholarship. Based on Macquarie University MRes thesis guidelines, the main body of the thesis is restricted to a maximum of 50 pages, approximately. The first objective of this thesis is to design highly transmitting 3D printable meta-atoms that can be used to control the phase of the propagating field. The second objective is to design phase manipulating surfaces through periodic arrangement of the meta-atoms. The third objective is to design a beam steering metasurface for RCA to be used for on-the-move wireless applications.

1.3 Thesis Overview

This thesis consists of six chapters including a brief introduction in Chapter 1 and concluding remarks documented in Chapter 6. The remaining 4 chapters are arranged as follows:

Chapter 2 comprises a literature review of artificial dielectrics, metasurfaces and 3D printing technology. Historical background, working principles and recent advances have been discussed with reference to all three aforementioned topics. The chapter emphasizes that artificial meta-atoms can be spatially arranged in an array to form a 3D printable metasurface which can be used for beam manipulation applications. Increasing demand and future market trends of additive manufacturing (AM)/3D printing have also been highlighted.

Chapter 3 is based on full wave simulations of meta-atom and parameters affecting their EM response. The design methodology of 3D printable meta-atoms with the ability to offer full transmission phase control and high transmission coefficient is presented. Phase gradient from the proposed meta-atoms is achieved by simultaneous variation of its three parameters, i.e dielectric constant, height and metal patch dimensions. Transmission characteristics of a metal patch mounted material (meta-atom) and pure dielectric have been compared to demonstrate the superiority of the former one.

Chapter 4 briefly explains the concept of phased array theory and mathematical relationships forming the basis of beam steering metasurfaces. The chapter presents the concept of phase wrapped metasurface design using a spatial arrangement of the meta-atoms presented in Chapter 3. Full wave simulations are used to demonstrate that electric field propagating in a direction can be deflected to any angle between 0° to 40° using plane wave source.

Chapter 5 is based on the demonstrating the application of metasurfaces. Proof of concept has been illustrated by the steering beam of medium gain RCA to a range of angles with less than 2dB variation in peak gain. Beam steering metasurfaces have been designed to work with a plane wave sources, so a permittivity gradient phase-correcting structure was also introduced to first transform the near-field phase distribution of the RCA. Peak gain of 21.65 dBi was recorded with sidelobe levels of -14.44 dB.

Chapter 2

Literature Review

In this chapter, we review the historical background of different aspects of the components related to this dissertation. The first part describes the potential of artificial dielectrics and some research advances related to them. In the later sections, we summarize the research carried out on metasurfaces and technological developments concerning 3D-printed structures.

2.1 Artificial Dielectrics

The history of material sciences and engineering is based on the creation of unique materials which are naturally non-existent. Electric metamaterials, commonly referring to materials with prescribed electric properties have been a subject of in-depth research since the 1940s. The electric and magnetic response of a medium can be expressed in terms of permittivity (ε) and permeability (μ), respectively [7]. Hence a core objective of studying electric metamaterials is to engineer metal-dielectric cells of the desired permittivity. They are commonly known as “artificial dielectrics”, because they constitute a macroscopic analogue of natural dielectrics including contaminations in the form of metallic atoms or molecules. These tailored materials also have the ability to mimic the local response of natural dielectrics. Since they are identical to natural materials, they have wide-spread applications in radio frequency engineering such as phase shifters, EM lenses and wave absorbers [8]–[11]. These materials with customized electrical characteristics have various names in the literature, and the most common terms used are meta-atoms and unit cells [12], [13].

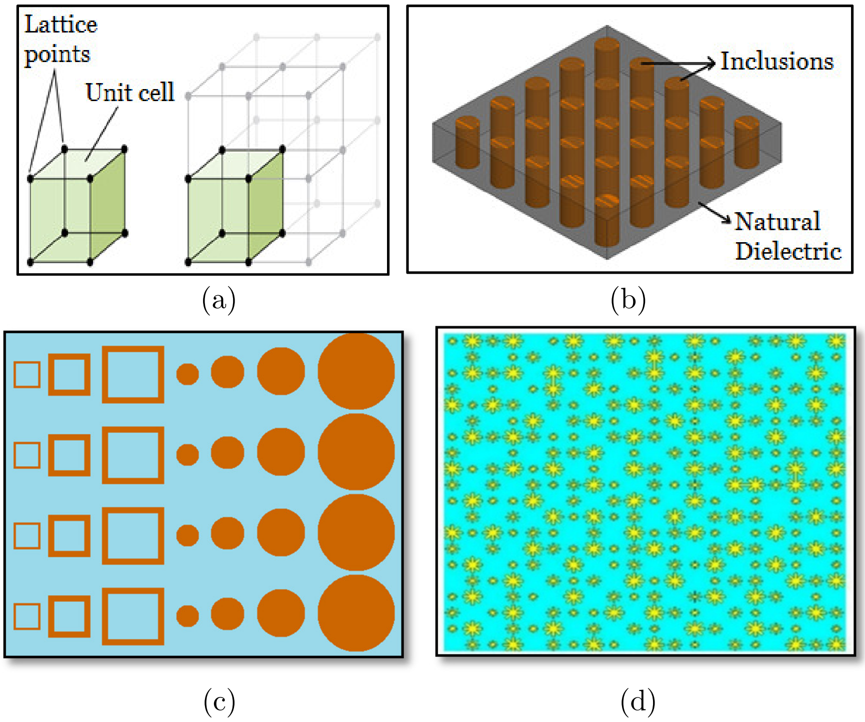

Figure 2.1: Classification of dielectrics (a) Regular lattice points in a unit cell (b) regular artificial dielectric with equi-spaced and sized spaced inclusions (c) random artificial dielectric with equi-spaced and variable sized inclusions (d) random artificial dielectric with unequally spaced and variable sized inclusions.

Over the years they have elicited inimitable properties in the microwave regime such as tailored permittivity and permeability. It has been identified that nano-structured composite dielectrics can possess unique properties in optical nonlinearity, reflectivity and emissivity [14]. Consequently, these tailored materials are recognized as having a more decisive role in the technological advances than that played by the artificial dielectrics in previous decades (in fact, for much of their existence which has been approximately 100 years). These synthesized substances offer greater flexibility as they offer properties that are non-existent in nature by including minor contaminations in naturally occurring materials. Based on their geometry, artificial dielectrics can be categorized into two kinds: regular artificial dielectrics and random artificial dielectrics. Figure 2.1 depicts the classification of artificial dielectrics and Table 2.1 compares both categories on the basis of various physical properties.

Table 2.1: Comparison of natural and artificial dielectrics on the basis of physical properties.

Sr. No.	Regular Artificial Dielectrics	Random Artificial Dielectrics
1.	Inclusions are dispersed homogeneously into the host material.	Inclusions are randomly dispersed into the host material.
2.	Regularity and repetition of lattice points result in replication of naturally occurring materials.	Isotropic in nature and does not replicate naturally occurring material.
3.	Easy to manufacture and mass production due to regularity in structure.	Complex irregular structure hinders mass production.
4.	Can be manufactured with a high degree of accuracy and consistency.	Random dispersion violates consistency and accuracy in manufacturing.
5.	Material characteristics vary in a controlled manner due to uniformity.	Material characteristics vary in unidentified ways.
6.	Homogeneous solid substances	Heterogeneous solid substances

Commercially available materials with high permittivity are usually expensive so an alternative approach to artificially attain their equivalent characteristics is required. This can be done by incorporating trivial metallic inclusions of variable shapes and sizes [15]–[17]. In this way high permittivity materials can be artificially synthesized, they are cost-effective and lightweight because the inclusions are small compared to the operational wavelength [18]. This leads us to the assumption that to attain desired permittivity and permeability from naturally existing materials, access to the atomic level is required. Variation in atomic arrangement produces alteration in the EM properties of materials and as a result their effective electric and magnetic parameters are changed. Some easily accessible scatterers based on this concept were manufactured in the late 1940s with the ability to mimic the response of natural substances. When a dielectric is exposed to an EM field, scattering occurs at the atomic and molecular level and resultant response of material is expressed in terms of electric permittivity and magnetic permeability. There are two requirements to make this response macroscopic: firstly, a spatial ordering is required between the scatterers; secondly, must be related in specific way to the wavelength of operation (i.e. inclusion must be very small compared to wavelength).

In the radio frequency and microwave domain, these artificially synthesized crystal lattice structures were assembled to attain desired permittivity and permeability values. Manually introduced scatterers respond to an EM field similarly to the way atoms and molecules behave in natural materials. Furthermore the response of complete substance replicates the response given by natural dielectrics.

2.2 Historical Development of Artificial Dielectrics

Kock initiated the idea of artificial dielectrics and used them at microwave frequencies to design light-weight dielectric lenses [19]. Since then artificial dielectrics have also been applied where high-permittivity materials are needed. During the 1940s, it was identified that propagation behavior of microwaves was similar to light waves in many aspects. From this it emerged that they can be focused using lenses made of certain materials like plastics, polyethylene and polystyrene. In the beginning, such lenses were employed in radar systems but they were considered too bulky because of their very large apertures (several feet in size). Consequently, synthesized lenses were acknowledged to be too bulky for such applications. Kock provided a solution to this issue by proposing that a stack of equi-spaced parallel conducting plates worked as a refractive medium and could be used as a lens. In later years, Kock manufactured a plano-convex lens using an artificial dielectric. This artificial dielectric consisted of trivial dielectric or metallic substances of arbitrary shapes regularly arranged in a 3D lattice. In the 1940s, the increasing demand for lens antennas proved to be an additional motivation for research in this area. The outcome was the development of lens antennas for various applications including outer space.

An interesting example of artificial dielectrics known since 1950s is robbed medium (wire medium) [20], [21]. It is composed of conducting wires of small radii arranged in a regular lattice structure. This structure possesses some unique non-resonant material characteristics and one of them is a negative permittivity over a wide frequency range. Various microwave technologies such as radar were used in the Second World War. Since then artificial dielectrics have largely come into use for military applications and enjoyed a remarkable development between the 1940s and 1970s [22], [23]. Figure 2.2 shows offshoots of artificial dielectrics that have been explored to date. In the 1950s and 1960s, these artificially engineered substances were explored for applications in lightweight microwave antenna lenses and absorbers. Referring to the 1980s and 1990s, artificially synthesized chiral materials were investigated for microwave absorbers and other applications. Propagation of EM waves in chiral media has been thoroughly discussed in the literature [24]–[26].

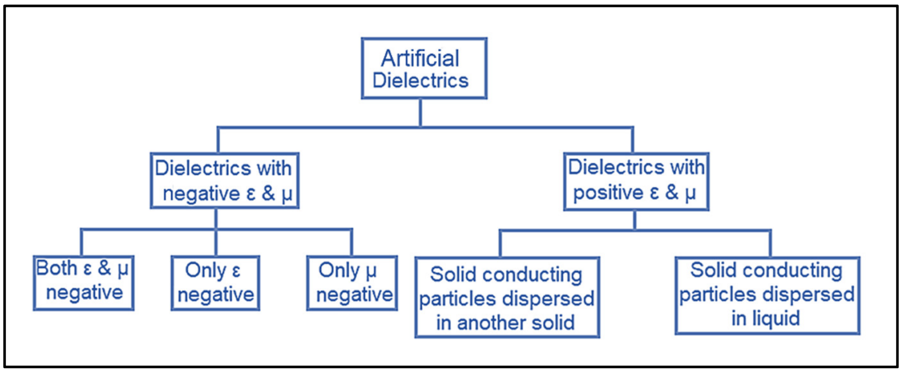

Figure 2.2: Overview of research development in artificial dielectrics in past 100 years

In recent years, artificial dielectrics have been used as phase and amplitude shifting structures (PASS), microwave lenses and holograms [27]. Moreover, the concept has expanded to fabricate multilayer meta-atoms to incorporate polarization and phase shift in incident wave by tuning the structure's parameters [28]. Recently, 3D-printed meta-atoms with enhanced relative permittivity have been presented. They had trivial metallic cuboid inclusions (much smaller than the wavelength of operation), spatially arranged in regular or irregular lattice of host dielectric material. Metallic inclusions resulted in an increase of relative permittivity generated by the host material and produced 3D printable metamaterials with tailored EM properties [13].

Artificial dielectrics can be arranged in a 2D configuration, like arrays of antennas with subwavelength inter-element spacing between adjacent elements to generate spatially varying responses. These spatially arranged cells can mould wavefronts into desired patterns because they are able to alter phase, scattering amplitude and polarization. The theory of phase gradient concerning tailored materials is based on the laws of transmission, reflection and refraction through them. So artificial dielectrics can be arranged in geometric order to form interface with the ability to impose phase shift on EM waves transmitting through them. This two-dimensional spatial arrangement of artificial dielectrics is commonly known as metasurfaces.

2.3 Electromagnetic (EM) Metasurfaces

The history of metasurfaces is closely linked to metamaterials, which constituted a topic of great interest up until the first decade of the 21st century. Metasurfaces are made out of metamaterial structures with subwavelength thickness, and operate at wavelengths ranging from microwave to visible. One of the most empirical applications of metasurfaces is wavefront control of EM waves by instilling phase gradient to the input wave. This leads to the concept of transmission and reflection through dielectric media and enables us to use metasurfaces for fabrication of EM lenses, polarization converters, spectrum filters absorbers and reflectors [29]–[31]. Arrangement of ultrathin meta-atoms with appropriate parameters supresses the undesired losses in the direction of propagation. Metasurfaces have the ability to reduce dependence on the propagation effect by introducing abrupt variation in EM properties. They also offer a degree of freedom in designing spatial inhomogeneity over thin interfaces. Through the years, metasurfaces have been used as polarization transformers, absorbers, wavefront manipulators and spatial filters. Recent research advances in metasurfaces has opened doors for their application in various useful EM applications. Many of these are recognized as promising alternatives of conventional devices, in that they can potentially overcome several limitations possessed by their traditional counterparts, and demonstrate versatile novel functionality. Figure 2.3 depicts some of the applications of metasurfaces.

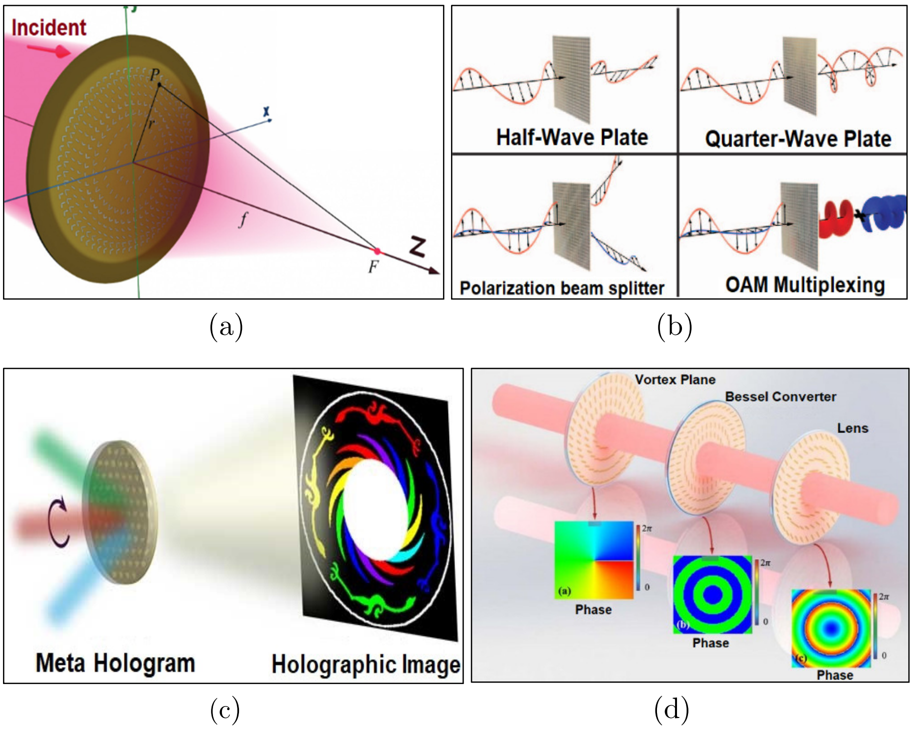

Figure 2.3: Metasurface based applications on polarization control and wavefront shaping (a) Planar lenses (b) Polarization transformers (c) meta holograms (d) Optical vortex converter.

A few challenges are evident in the fabrication of metasurfaces, principally the difficulty in fabricating micro- and nano- three dimensional structures using traditional machining techniques like lithography and nano-printing. Various fabrication methods have been tried in the past to develop metasurfaces that provide desired phase shift $[0, 2\pi]$ while at the same time keeping the transmission magnitude high. 3D printing is a rapidly growing applied synthesizing technique with the advantages of being cost-effective, rapid, automated, and repeatable. It can produce extremely customisable metasurfaces for state-of-the-art applications. Heterogeneous metamaterials with modified geometries can be efficiently manufactured by the AM technique. Such materials are difficult to fabricate using traditional micromachining. In the following section, we will discuss trends and advantages of the 3D printing technology.

2.4 Advances in 3D Printing Technology

3D printing, also termed AM or FDM (fused deposition modelling), is a novel manufacturing process, in which material is joined or solidified under computer control to synthesize three-dimensional structures. In this process, objects are formed by creating successive layers of material. Structures of arbitrary shape and geometry can be produced using digital 3D modelling data or any alternative electronic data source like an Additive Manufacturing File (AMF) file [32], [33]. The origin of the term 3D printing makes sense as it alludes to a procedure that adheres a binding agent to a powder bed using inkjet printing in successive layers. 3D printable model files can be created with computer-aided design (CAD) software, using a scanner or by a simple digital camera and photogrammetry software. CAD produced 3D-printed models result in less errors and offer the opportunity to amend a design by highlighting possible errors prior to printing. This process of modelling to produce geometric data for 3D computer graphics can be related to plastic arts such as sculpting. The 3D scanning stage collects digital data a physical object's geometry and appearance by generating a digital model based on its shape. Prior to printing, the generated Standard Tessellation Language (STL) file of the model must be examined for errors. Most CAD software generates errors, for example intersections in models, manifold edges, faces normal and holes in output STL files. These errors are fixed by a "repair" function in STL generation. Usually, STLs generated from a model obtained using 3D scanning have more of these errors. This is because 3D scanning works on a point-to-point acquisition principle, so the resulting model will include errors in most cases. Once the errors are repaired the STL file is processed by a piece of software termed a "slicer". During this phase the model is converted into a series of thin layers and a G-code file comprising commands tailored to the particular type of 3D printer (FDM printers) is generated. The resultant file can then be printed using 3D printing client software (that loads G-code and uses a set of commands to instruct the 3D printer during the printing process).

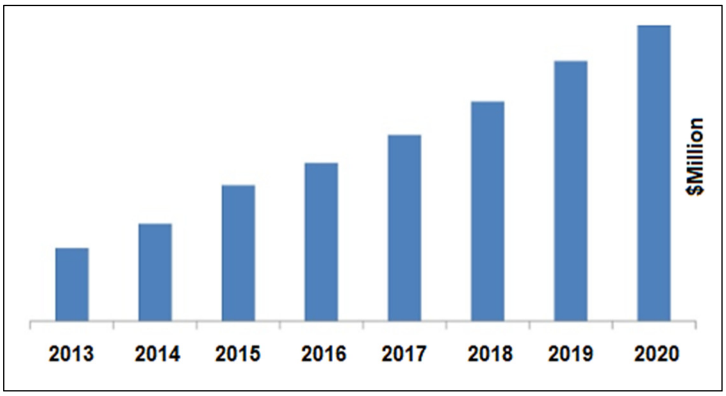

Figure 2.4: Commercial growth of the 3D printing market since 2013 and expected future forecast estimated as million $ investment per annum [34].

The printing resolution (expressed in micrometres (µm) or dots per inch (dpi)) and the layer thickness depend on the printer resolution. A typical layer thickness is approximately 250 dpi (100 µm), but some printers have a printing capability of as thin as 1600 dpi (16 µm). Every printed dot has a diameter of around 510 to 250 dpi (50 to 100 µm) and the X-Y resolution is equivalent to that of laser printers. Modelling setup using contemporary methods may take from several hours to several days, depending on the technique used, and the complexity and size of the structure. AM systems typically abate this time to a few hours, even though it varies depending on the modelling machine type and the size of the structure. Customary methods such as injection moulding are cost-effective for synthesizing polymer products in bulk quantities, but AM is deemed to be more flexible, faster and less expensive when fabricating comparatively small quantities of objects. 3D printing technology enables concept development teams to produce models using a desktop printer.

A great amount of work has been done on 3D printing in recent years, which will be summarized in the next subsection. In 2017, additively manufactured, artificial meta-atoms with metallic cuboid inclusions in a host dielectric were presented [35]. The EM parameters (permittivity and permeability) of the new material were numerically analysed, which confirmed that injection of metal into a dielectric alters its EM properties. In 2016, a flat graded-index (GRIN) lens was developed out of materials which were difficult to find commercially. The lens was designed to transform a spherical wavefront into a planar wavefront and vice versa. It comprised materials with tailored permittivity values [36]. The GRIN was light-weight, cost effective and marked improvement on the traditional lenses. 3D printing enabled fabrication of an entire lens in a single process lasting 4-5 hours without any intervention of machining or manual assembly. The total weight of GRIN was approximately 130 grams.

2.5 3D Printing Trends

Numerous radio-frequency (RF) components such as frequency-selective surfaces (FSS), lenses and waveguides have been fabricated using FDM, which are cost-effective and offer extra design freedom compared with conventional techniques [37]. Moreover, because it needs no bonding and machining, this fabrication method adds to the physical robustness of the product [38],[39]. 3D printing has wide-spread applications, in manufacturing, architecture, medicine, and customized art and design. Currently, the 3D printing technology is being used in the manufacturing, industry, medical and sociocultural sectors, which makes it a successful commercial technology. Based on present trends, it has been observed that 3D printing is becoming more easily accessible and affordable, and it is speculated that the cost of such designs will fall even more in the future. Figure 2.4 shows the trends in 3D printing technology from 2013 to the early 2020s. It is clearly evident that the market's annual revenue is irresistibly rising.

According to a study conducted by Grand View Research, Inc. based on the compound annual growth rate (CAGR), an annual expansion of 15.6% is estimated from 2014 to 2020 and by the end of the second decade of the 21st century, the market is expected to hit its highest ever total of US$ 1,129.8 million. Increasing industrial interest, a vast variety of materials, improvements in technology and more advanced 3D printers are the main reasons for this expansion of the market. The strongest growth is expected in the aeronautics and medicine/medical services industries. Other expected engines of growth are increasing general public interest and the automobile industry. Global Market Insight has forecasted that revenue generated by 3D printing will escalate further in the coming years and may possibly rise to a billion-dollar industry by 2024 with a CAGR of 17%.

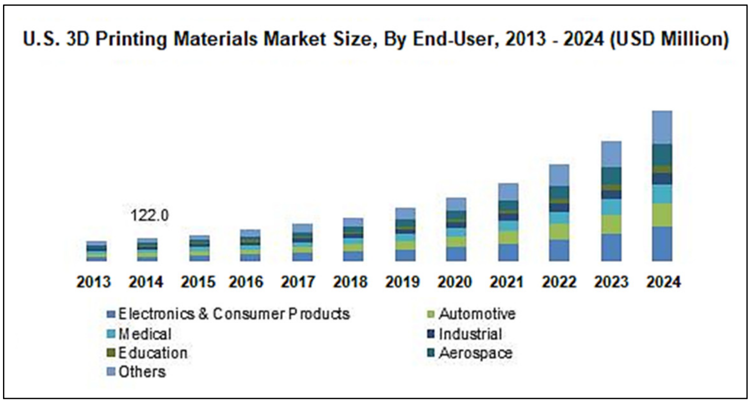

Figure 2.5: Future demand of 3D printing in various industries [40].

These predictions are based on the growing needs for AM products such as ceramics, plastics, and metals to be used in automotive, medical, industrial, education, aerospace, electronics and consumer products. Figure 2.5 illustrates the expected future demand for 3D printing technology in various industries. Because of the significant use of metal in aerospace, defence and automotive industries, the 3D printing material market's size will also expand. Factors involved in 3D printing can positively impact on industrial demand as they offer rapid prototyping. In 2015, the 3D printing materials market' was led by North America, accounting for 35% of the global industry. Between 2016 and 2024, the Asia-Pacific region is likely to witness maximum growth due to the increasingly robust and outreach of the automotive manufacturing in countries like Japan, China, India and Indonesia. Figure 2.6 depicts the segment growth during the forecast period up until 2024.

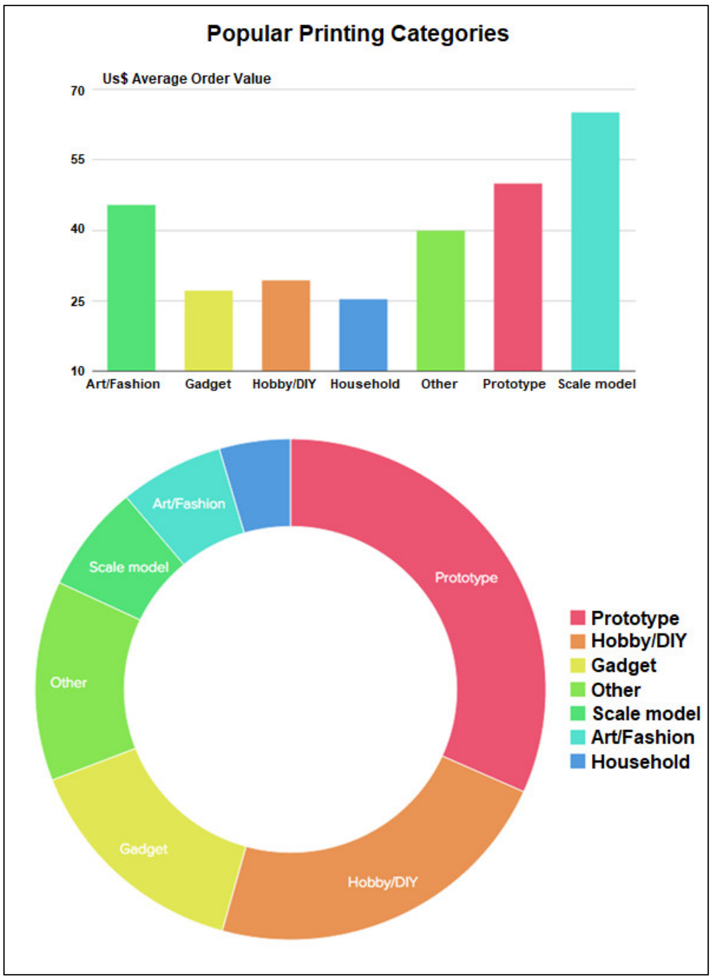

Figure 2.6: Popular printing categories represented in bar chart form depicting the average order value in US$; and pie chart indicating the popularity of demand in various industries [41].

Chapter 3

3D Printable Meta-Atoms

3.1 Introduction

A generalized overview of artificial dielectrics, metasurfaces and 3D printing has been presented in Chapter 2. This chapter is concerned with 3D printable meta-atoms having the ability to offer full phase manipulation with an extremely small reflection coefficient. The proposed meta-atoms/unit cells are an intermediate between all dielectric and all metal phase manipulating structures which have their respective limitations pertaining to excessive height and ohmic losses, respectively. Meta-atoms are smaller in height compared to all dielectric cells and offer higher magnitude of transmission coefficient compared to all metal cells. Phase variation from the proposed meta-atoms is achieved by simultaneous alteration of three parameters (dielectric constant, height and patch dimensions) of the cell which were discovered by extensive parametric analysis.

This chapter seeks to realize the first objective of dissertation, i.e. design a highly transmitting 3D printable meta-atom that can be utilized to control phase of the propagating field. The chapter is organized into following sections. Section 3.2 highlights design specifications for contemporary 3D printable structures and constraints related to modern day 3D printing technology. Section 3.3 describes the steps involved in simulation of a meta-atom. Parametric analysis of important design parameters such as transmission magnitude and phase shift of the structure are discussed in sections 3.4 and 3.5. Achieving full phase control [0-2π] is vital to ensure meta-atoms are useable for various beam manipulation applications (see section 3.6). To highlight the superiority of 3D printable meta-atom, a comparison with all dielectric cells is presented in section 3.7.

3.2 3D Printing Design Specifications

Over the years, PLA (Polylactic acid) and ABS (Acrylonitrile Butadiene Styrene) have been the two most common FDM printing materials. They are both low-cost thermoplastics with respective dielectric constant values of 2.72 and 3.1. In more recent work, new materials like polymers and metals have also been explored for 3D printing. Modern day printers enable printing of ceramic materials which increases options not only in terms of material selection but also broadens the permittivity range available for fabrication. Currently, the available dielectric constant range is from 1.1 to 8.0 and height of material can be an arbitrary thickness from 0.1 mm to a few centimetres. These specifications were stated by a world-leading additive manufacturing company that has expertise in material sciences, SYMETA (Loughborough, UK). A proposed structure will be fabricated in the company's facility in the coming years.

It makes 3D printing superior to fabrication using traditional materials which are commercially available with particular thickness and discrete permittivity values [42]. Using 3D printing, any material within the aforementioned ranges of permittivity and thickness can be fabricated. Moreover 3D printing is low-cost as it requires normal thermoplastics, polymers and ceramics to be melted and printed using a 3D model. To make metal and dielectric meta-atoms, a metallic patch of aluminium or stainless steel with a thickness greater than 100 µm (or 0.1 mm) can be mounted on the surface of a dielectric.

3.3 Meta-Atom Configuration

This study presents the simulation based design and analysis of multi-layer metal and dielectric artificial materials (can be termed as meta-atom or unit cell) having a square metallic patch mounted on a host dielectric material. These materials can be additively manufactured with a FDM 3D printer. Such an application is to use these materials to manipulate the phase of the propagating electric field. Meta-atom is a fundamental unit of the phase manipulating surface. It is designed using full wave simulations referred to in the literature as a unit cell simulation. This is achieved by imposing periodic boundary conditions along lateral directions of a meta-atom. An example of a periodic metasurface is shown in Figure 3.1, which is made of meta-atoms by their repetition in lateral directions.

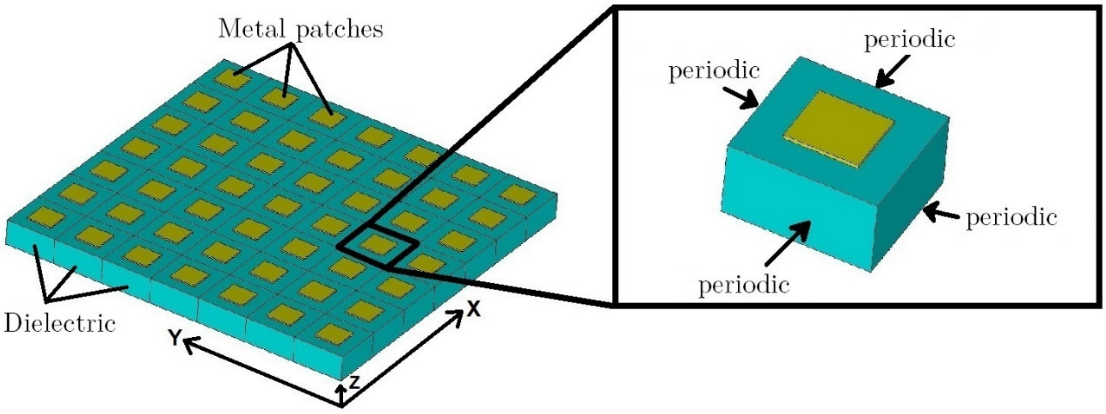

Figure 3.1: Metasurface with periodic meta-atoms in lateral directions x and y. Zoomed region shows configuration of a single meta-atom with periodic boundaries in x and y axis.

Meta-atom is the fundamental unit of metasurfaces which can be used for various beam-forming applications. Figure 3.2 shows proposed 3D printable meta-atom considered in this thesis. Its dimensions will be discussed in later but it is important here to introduce physical parameters marked in the figure. Based on specifications obtained from fabrication facility, the height of the metallic patch is fixed to 0.1 mm i.e. H_p=0.1 mm. The height of the dielectric, D_h is a variable that can have any value between 0.1 and 8.0 mm. D_p is dielectric periodicity, which is constant length of dielectric block in the xy-plane. Metal patch (copper) of size P_s is mounted at the top and bottom of the dielectric block. Patch was considered to be square in shape so it has the same length in lateral directions which resulted in reduced unknowns. Variation concerning the size of the rectangular patch requires two variables but the square patch has only one variable. Moreover, this square patch has an identical response to orthogonal polarizations. Square meta-atom can be used for circular polarization applications because it exhibits 90° degree rotational symmetry. The dielectric constant (ε_r) of the meta-atom's substrate is also a variable which can vary from 1.1 to 8.0 as per specifications provided by SYMETA. Dielectric periodicity (D_p) of 5 mm ($\lambda_o/3$) was constant in lateral directions and it was selected on the basis of wavelength (15 mm in this case). This dielectric periodicity size helped to reduce simulation time by creating simpler mesh.

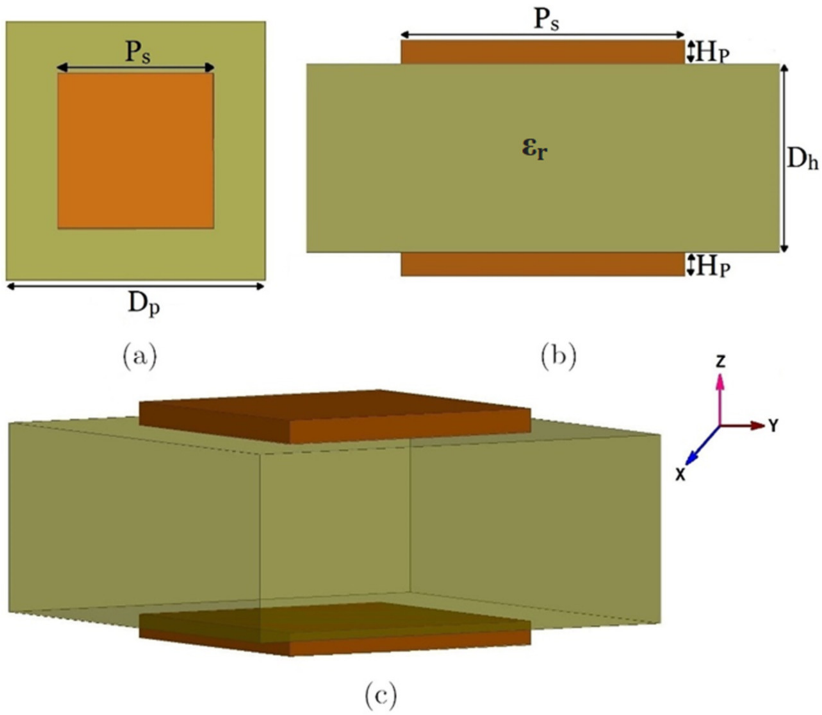

Figure 3.2: Meta-atom structure comprising dielectric sandwiched between two layers of metal (three layer structure) (a) Top view. (b) Side view. (c) 3D view.

In the simulation process, the conductive patch was assumed perfectly conducting while the dielectric material was deemed to be lossless. To finalize the configuration, an air box was introduced on the top of the meta-atom. The objective of introducing this air box was to ensure the input and output planes were at a fixed distance, irrespective of the value of D_h. Because of the variation in the substrate height, final spatial arrangement of meta-atoms in form of a metasurface will look non-planar so while designing meta-atom, an air distance of a few millimetres is required in order to create an even output plane. Transmission magnitude and phase were recorded at the output plane to attain characteristics of media at planar surface [43]. Total height of the cell was retained at 21 mm while the height of the air box varied with respect to variation in dielectric height. Figure 3.3 shows complete configuration of the proposed 3D printable meta-atom with air box at the top.

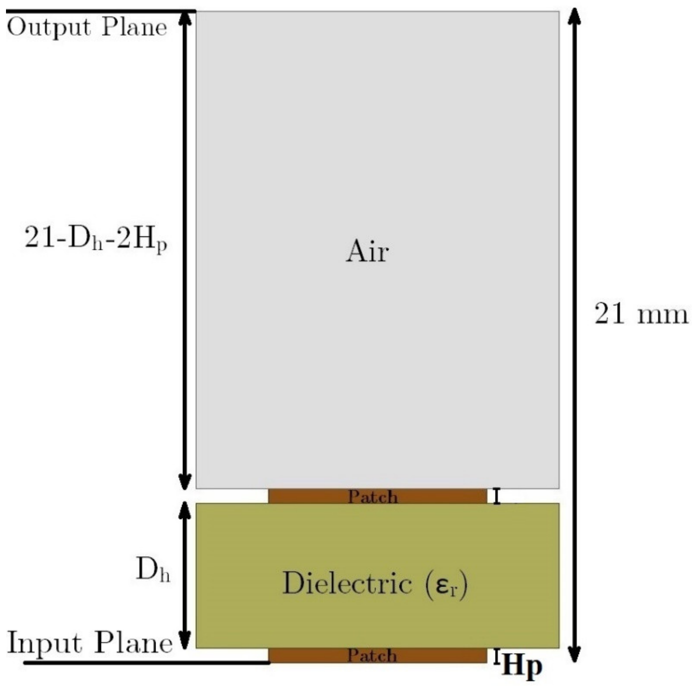

Figure 3.3: Meta-atom with air box at the top with input and output planes marked.

For simulation of a unit cell, HFSS (high frequency structure simulation) software offers master-slave boundary conditions to realize periodic boundary conditions. The boundary conditions at the master are enforced at the slave's surface, hence realizing an infinite periodic repetition. This method is effective for the cubic unit cell for which a master boundary condition can be assigned by selecting an appropriate side of the cube. For each slave boundary to be assigned the corresponding master boundary needs to be specified. After assigning boundary conditions and excitations to the structure, analysis setup is specified including the operating frequency (20 GHz in this case), and the meta-atom was simulated.

Parameters of interest, magnitude and phase of transmission coefficient were extracted from post-processing. The prime focus is to discover physical parameters of the cell, variations of which can yield complete [0-2π] phase shift while maintaining a high transmission magnitude. Mounting the metal patch on the dielectric increases its permittivity and results in amplitude and phase shift different to that of a pure dielectric slab (bare dielectric). Equivalent permittivity value depends on the patch size but it also means the cell transmits less because with an increase in metal patch size, the reflection coefficient increases [44]. Consequently, there is a limit to the permittivity value we can achieve utilizing the aforementioned approach. If the required patch size becomes comparable to the local periodicity of the unit cell, the magnitude of the transmission coefficient becomes too low for a phase manipulating metasurface.

To investigate phase shift for the meta-atom, a reference phase was recorded for bare dielectric (dielectric with no patches) and it exhibited the normalized phase shift of 0°. Later on two different configurations were considered to explore the effect of altering different variables associated with the meta-atom. The first configuration has two layers one metal and one dielectric whereas the second configuration comprised one dielectric layer sandwiched between two metal layers.

3.4 Two Layer Meta-Atom

The first configuration considered in the attempt to find a relationship between magnitude and phase of transmission coefficient consisted of a single patch mounted on top of the dielectric block. This henceforth was referred to as the two layer meta-atom. In this case the arrangement is similar to that shown in Figure 3.2, but with only one patch at the top. Three physical parameters, dielectric height (D_h), patch size (P_s) and dielectric constant (ε_r) were investigated to explore interdependence of phase and transmission magnitude. For clarity of expression, during parametric analysis all three parameters were not varied at once. Instead an analysis was done by keeping one of them fixed while the other two were altered.

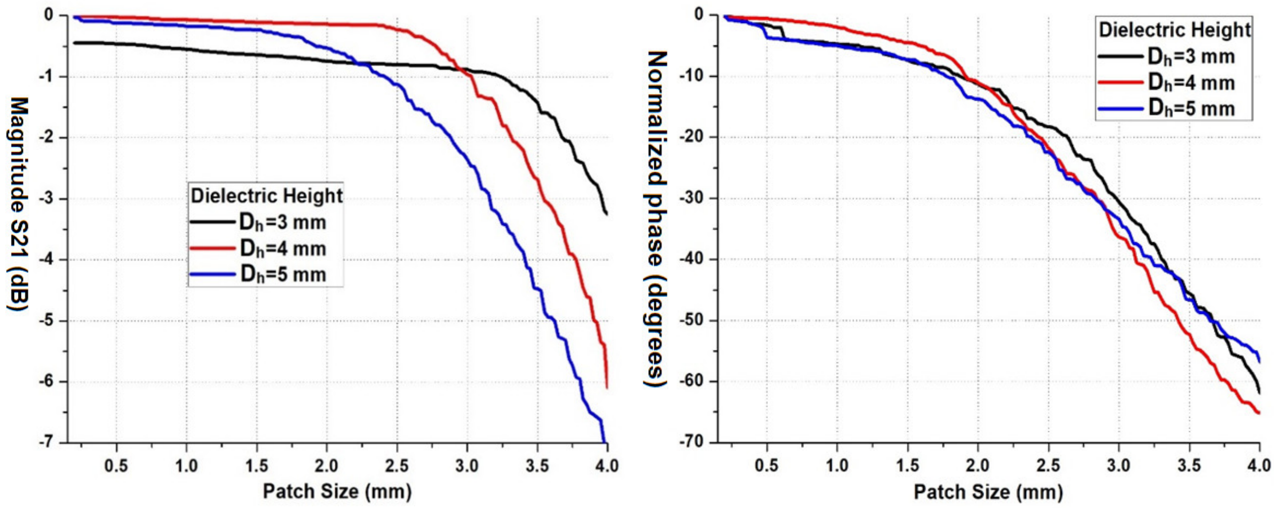

(a) (b)

Figure 3.4: Simulated transmission results for two layer meta-atom with dielectric height variation from 2 mm to 5 mm, dielectric constant of 2.72 and patch size from 0.1 mm to 4.0 mm (a) magnitude versus patch size (b) normalized phase versus patch size.

3.4.1 Two Layer with Fixed Dielectric Constant

Dielectric constant (ε_r) had a fixed value of 2.72 while the height of the dielectric varied from 2.0 mm to 5.0 mm with step width of 1.0 mm and patch size ranged from 0.1 mm to 4.0 mm with step of 0.1 mm. Magnitude and phase of transmission coefficient was recorded and it was revealed that both were interdependent, while for higher phase shifts, transmission magnitude becomes very low and vice versa. Figure 3.4(b) shows that the obtained phase range is very marginal; it is maximum when the height is 4.0 mm, i.e. ≈ 65° (symbolized by red line) for the complete patch width variation. If transmission magnitude ≥ -3.0 dB is considered from Figure 3.4(a), for the corresponding patch size of 3.5 mm the achieved phase shift further decreases to 53.5° in Figure 3.4(b). Similarly for the substrate height of 5 mm (blue line representation), the total phase shift achieved is ≈ 55° but for the case of transmission magnitude greater than -3.0 dB, only patch variation up to 3.0 mm is permissible. This equates to corresponding phase shift of 35°. It proves that a single square conductive patch on top of the dielectric (with variable height within 3D printing range) is not sufficient to attain significant phase shift. Furthermore it cannot serve in beam-forming applications as they require complete 2π phase gradient.

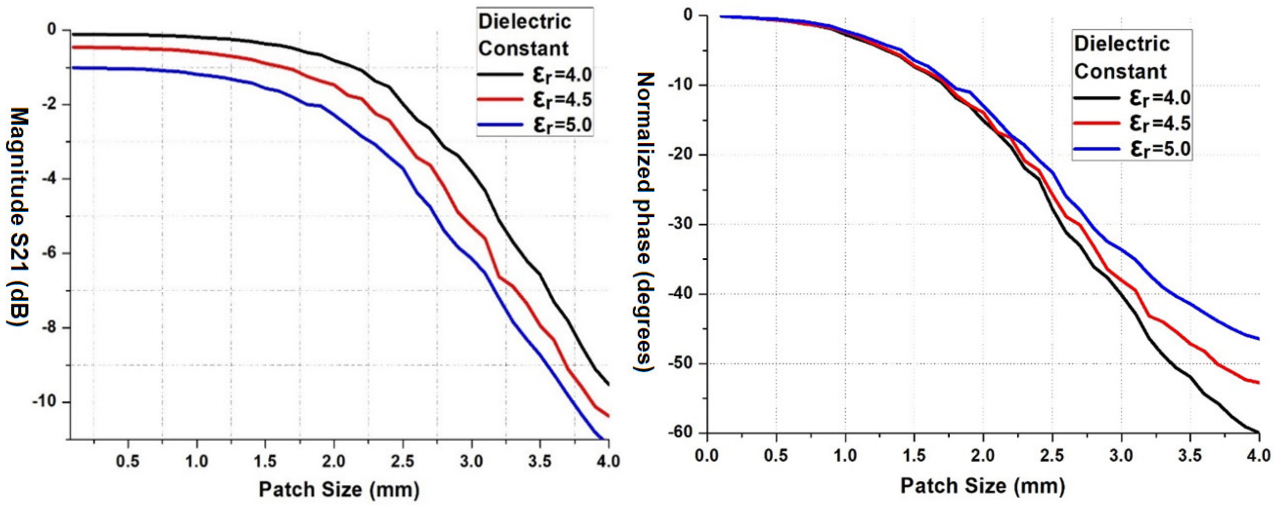

(a) (b)

Figure 3.5: Simulated transmission results for two layer meta-atom with dielectric constant variation from 4.0 to 5.0, constant height of 3 mm (a) magnitude versus patch size (b) normalized phase versus patch size.

3.4.2 Two Layer with Fixed Dielectric Height

The second parameter that was investigated to determine transmission magnitude and phase shift was the dielectric constant (ε_r). The ε_r varied but the height remained constant. In this case the height was fixed at 3.0 mm, while the dielectric constant was varied from 4.0 to 5.0 with step of 0.5 and patch size ranged from 0.1 mm to 4.0 mm by step width of 0.1 mm. Dielectric constants with a smaller value showed negligible variation in phase and magnitude so this particular range was selected to elaborate the concept. Figure 3.5(b) demonstrates that the obtained phase shift reaches its maximum for the dielectric constant for 4.0 (represented by the black line) and minimum for 5.0 (represented by the blue line) i.e. ≈ 60° and 47°, respectively, for the complete patch width variation. If transmission magnitude of ≥ -3.0 dB is considered from Figure 3.5(a), for the corresponding patch size of 2.3 mm and 2.9 mm the achieved phase shift further decreases to 18.5° and 30° for dielectric constant of 4.0 and 5.0 respectively. Results suggest that the dielectric constant of the slab is another parameter that greatly affects transmission magnitude and phase variation. However, it did not return significant phase gradient so modifications were made to make it useful for beam-forming applications.

3.5 Three Layer Meta-Atom

In the second configuration, a dielectric block was sandwiched between metal patches having a thickness of 0.1 mm (see Figure 3.2(b)). To reduce simulation time and computer memory requirements, conductive patches at the top and bottom of the dielectric block were altered using the same variable in optimetrics.

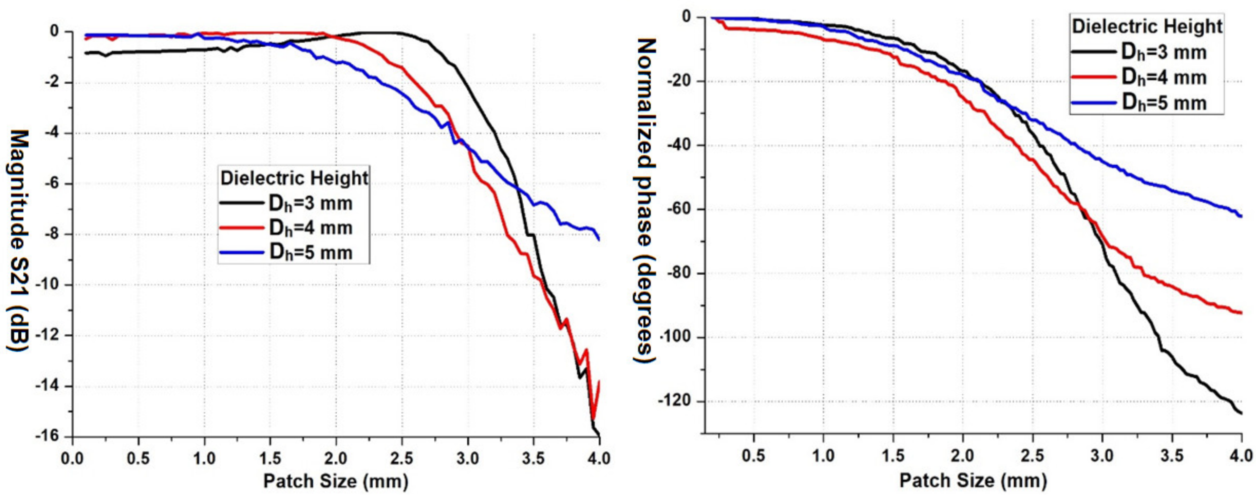

(a) (b)

Figure 3.6: Simulated transmission results for three layer meta-atom with dielectric height variation from 2 mm to 5 mm, dielectric constant of 2.72 (a) magnitude versus patch size (b) normalized phase versus patch size.

3.5.1 Three Layer with Fixed Dielectric Constant

Similar to the previous two layer meta-atom case, the transmission magnitude and phase shift cannot be tuned independently, yet the shift range obtained for the three layer case was significantly better than for the two layer case scenario. Figure 3.6(b) shows that the obtained phase is improved compared to the case of one patch configuration, and it is maximum for the height of 3.0 mm i.e. ≈ 125° (represented with black line) for the complete patch width variation. If transmission magnitude of ≥ -3.0 dB is considered from Figure

3.6(a), for the corresponding patch size of 3.05 mm the achieved phase shift further declines to 82° in Figure 3.6(b). Similarly for the substrate height of 4.0 mm (red line in Figure 3.6(b)), the total phase shift achieved is ≈ 95° but for the case of transmission magnitude greater than -3.0 dB only patch variation up to 2.8 mm is allowed. This equates to a corresponding phase shift of 60°. Evidently, it was still not sufficient to cover the desired range of 360° while maintaining high magnitude of transmission coefficient.

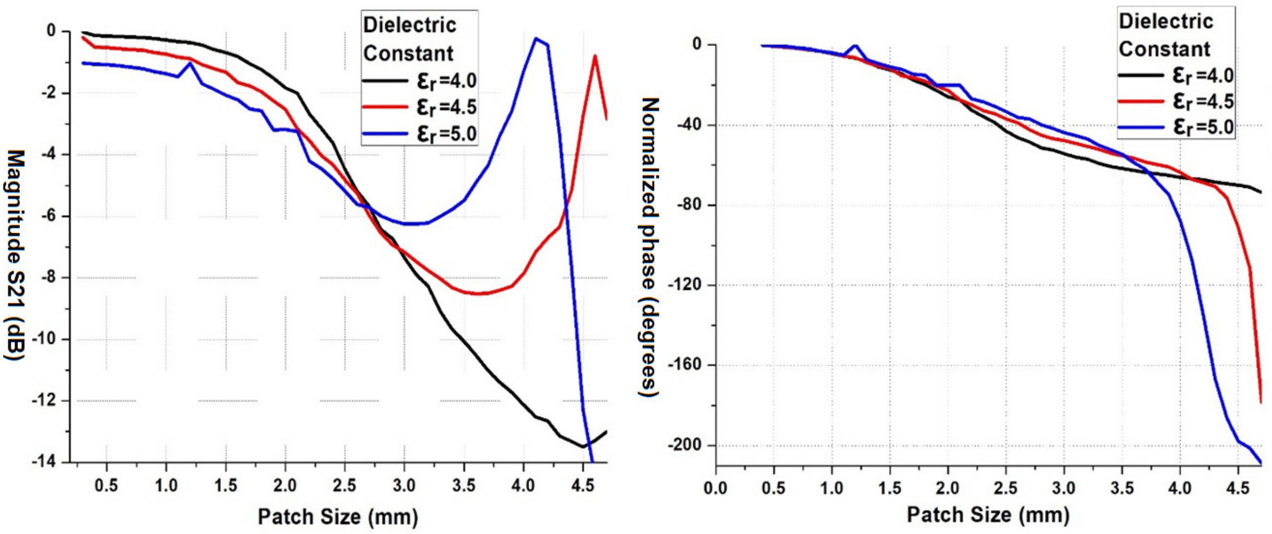

(a) (b)

Figure 3.7: Simulated transmission results for three layer meta-atom with dielectric constant variation from 4.0 to 5.0, constant height of 3 mm (a) magnitude versus patch size (b) phase shift versus patch size.

3.5.2 Three Layer with Fixed Dielectric Height

Dielectric constant variation with constant height of three layer cell indicated aberrant trends. Alteration in parameters was the same as the two layer case with a fixed dielectric height. In previous sections this has been explained as follows. Increasing the patch size means the transmission magnitude decreases but in this case high values of transmission coefficient were achieved even for bigger patch size, i.e. up to 4.7 mm. Figure 3.7(b) depicts an exponential increase in phase shift being achieved when patch size is bigger than 3.75 mm for ε_r of 4.5 and 5.0. In Figure 3.7(a) corresponding transmission magnitude for this range of patch size confirms that higher transmission coefficient is achievable with a larger patch for higher values of permittivity. For dielectric constant of 5.0 (blue line), phase shift of 220° is achieved and for 4.5 (red line) phase gradient is 175°. We can therefore assume that for range of permittivity, three layer meta-atom can offer high transmission magnitude. So dielectric constant values available for 3D printing can help to achieve the desired goal of 2π phase shift with a low reflection coefficient.

Table 3.1: Comparison of parametric analysis of two and three layer meta-atoms in terms of phase shift achieved.

		Phase shift for full patch size	**Phase shift for magnitude>-3 dB**
Two Layer meta-atom	Fixed dielectric constant	65°	53.5°
	Fixed height	60°	30°
Three Layer meta-atom	Fixed dielectric constant	125°	82°
	Fixed height	220°	130°

3.6 2π Phase Range Control

After completing the parametric analysis of two layer and three layer meta-atoms, it was inferred that the latter offered superior phase gradient by alteration of physical parameters. Table 3.1 summarizes the comparative analysis of both cells. More complex meta-atom structures with four and five layers have been reported in the literature but they use traditional machining techniques like lithography and printing; furthermore the designs are not valid for 3D printing [27]. The next step was to achieve a full phase gradient range [0-2π] using parameters that affected transmission magnitude and phase, the aim being to make cell useful for various beam-forming applications.

Three parameters were identified exerting the most influence on both aforementioned parameters of interest, i.e. dielectric height, dielectric constant and metal patch size. Variation of these causes a shift in transmission and reflection characteristics of cell in media which in turn offers a phase shift. The transmission and reflection through dielectrics and its effect on magnitude and phase shift have been discussed in detail in other studies [43], [45]. A better understanding of transmission and reflection can be developed by investigating transmission and reflection through pure dielectrics (see Appendix A). In the study of pure dielectric unit cell no metallic patches were involved, but their effect on variation of phase shift has already been discussed in sections 3.4 and 3.5. However, few patch mounted cells have been studied [46],[27]. We conclude that to achieve 2π phase shift (full phase range) with a high transmission coefficient, we can sweep dielectric height, dielectric constant and patch size within the available 3D printing range for all three parameters.

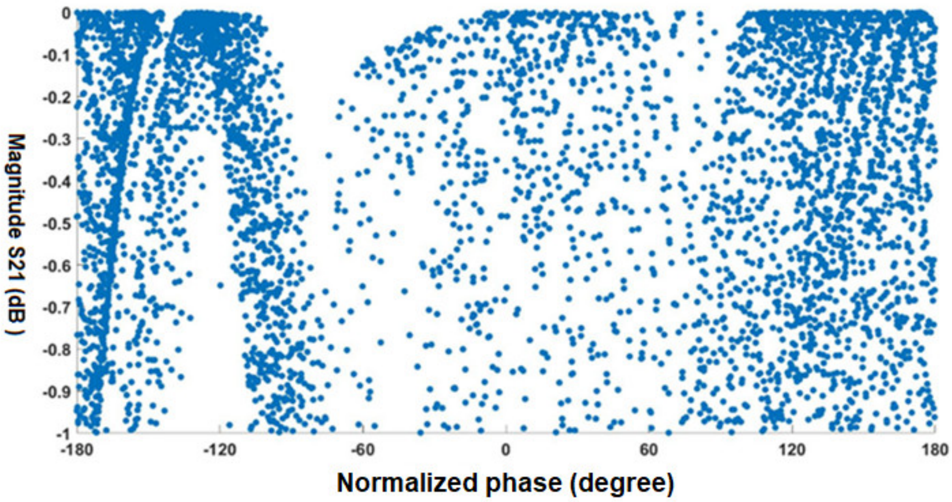

(a)

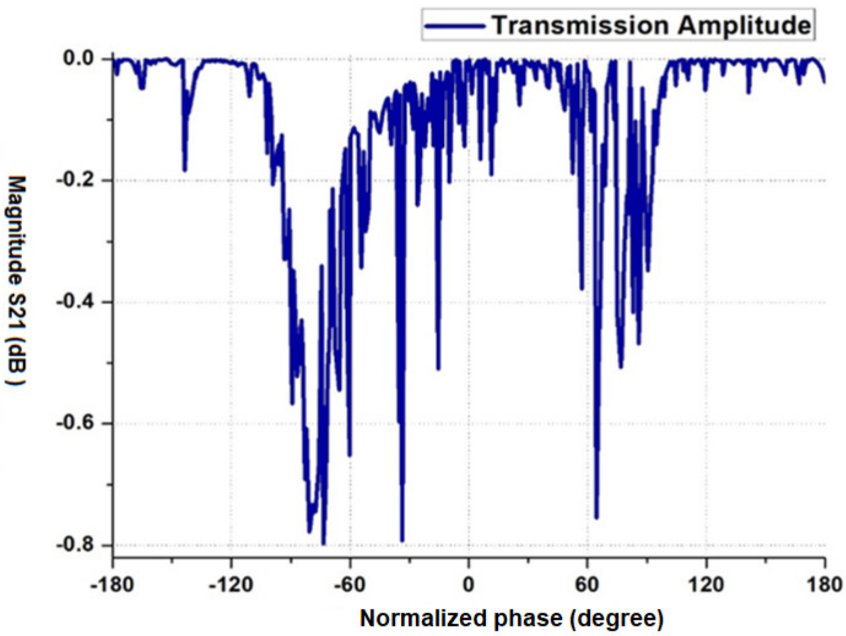

(b)

Figure 3.8: Simulated transmission results for three layer meta-atom with optimetrics mentioned in table 3.1 (a) 360° phase shift for magnitude>-1 (b) Best case of amplitude, i.e. all points covered for magnitude>-0.75 dB

In HFSS simulations, the optimetrics were added for variation of dielectric constant, dielectric height and patch size. Dielectric constant was varied from 1.1 to 8.0 with increment of 0.3. Dielectric height values were swept from 0.3 mm to 7.8 mm with a step of 0.3 mm and patch size varied from 0.5 mm to 3.8 mm with the same increment. Simultaneous variation of three parameters created a set of 7488 points which provided 360° phase shift. A database containing these points was stored in the form of a .csv file which provided information regarding variation of transmission magnitude and phase with changes in three optimetrics parameters.

Table 3.2: List of parameters used for simulations of unit cell to attain 360 phase gradient

Parameter	**Start value (mm)**	**End value (mm)**	**Step**
Dielectric Constant (ε_r)	1.1	8.0	0.3
Dielectric Height (D_h)	0.3	7.8	0.3
Patch size (P_s)	0.5	3.8	0.3
Dielectric Periodicity (D_p)	5.0		Constant
Patch height (H_p)	0.1		Constant
Air region	13	21	D_h dependent

Particular significance was given to full phase shift [0,2π] because cells with this ability can be used for beam-forming applications when arranged in phased array geometry. This theory is explained in more detail in section 4.2. It was retained due to the consideration that all variations were within the limitations of modern day 3D printing mentioned in sections 3.2 and 3.3. Figure 3.8(a) shows the full phase gradient achieved by simulation. Values from each point with the highest transmission magnitude are joined in form of a line plot in Figure 3.8(b), which shows that all points are covered in the > -0.75 dB transmission magnitude. Table 3.2 shows added optimetrics to achieve full phase gradient and dimensions of unit cells highlighted in Figure 3.2. Table 3.3 reports some phase values achieved by corresponding meta-atom dimensions and transmission magnitude. For example, if we want to attain phase shift of 150°, from the optimetrics database we can pick a point corresponding to this phase value. As listed in the table below, we require a dielectric slab with the height of

4.8 mm and dielectric constant of 2.3 with a metal patch 1.3 mm in size mounted on either side. Similarly, other values can be picked from the database of variables which promise that magnitude of the transmission coefficient will never go lower than -0.75 dB. To the best of our knowledge, to date this value is the highest ever demonstrated by the proposed highly transmitting meta-atoms.

Table 3.3: Some phase values with respect to corresponding dimensions of unit cell.

Phase value (degree)	Dielectric constant (ε_r)	Height of Dielectric (mm)	Patch size (mm)	Magnitude (dB)
50°	4.1	6.0	2.1	-0.46407
100°	4.7	2.1	2.5	-0.2914
150°	2.3	4.8	1.3	-0.02845
200°	1.4	3.3	0.7	-0.11781
250°	6.5	8	2	-0.01935
300°	6.9	3.6	3.4	-0.45709
350°	5.6	5.4	2.3	-0.33204

3.7 Comparison with All Dielectric

Figure 3.8(a) and Figure 3.9 help to realize 360° phase shift against transmission magnitude change for patch mounted cells and all dielectric cells respectively (pure dielectrics slabs with no patches). As mentioned in section 3.1, the proposed patch mounted cell configuration is superior to all dielectric cells [47]. The 360° phase shift was achieved by patch mounted cell using optimetrics as stated in Table 3.2 with a transmission magnitude greater than -0.75 dB. The same parameters were applied to all dielectric cells but this did not lead to a return phase shift of 360°. For all dielectric unit cells, full phase gradient was achieved by permittivity variation of 1.1 to 8.0 and height variation from 0.3 mm to 14 mm. This confirms that the patch mounted cell is superior because it achieved full phase shift with relatively lower maximum height value (height variation from 0.3 to 7.8 mm). In the case of height variation from 0.3 to 7.8 mm for all dielectric unit cells, phase points between 30° and 100° were missing. Figure 3.9 shows the achieved phase gradient by all dielectric cells with the region of missing points highlighted. Demonstrated here is the superiority of metal mounted cells in terms of achieved gradient.

Transmission characteristics were compared for both cells at some discrete values which inferred that all dielectric cells required higher permittivity or height to achieve equivalent characteristics of patch mounted cells. The cases for maximum height concerning the proposed meta-atom and all dielectric cells were compared, revealing that the three layer meta-atom is ≃44.3% smaller in height than all dielectric ones. This concept of mounting a patch on a pure dielectric is similar to dial-a-dielectric in which the patch is mounted on the dielectric to create s new material with desired transmission characteristics and its resultant relative permittivity is higher than the host dielectric [48], [49].

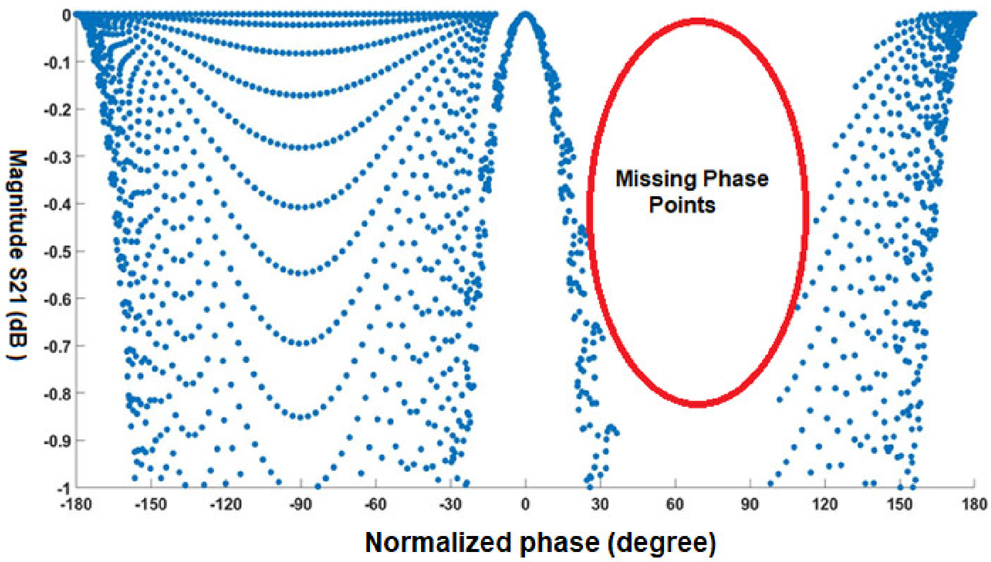

Figure 3.9: Simulated transmission results for all dielectric unit cells with dielectric height and dielectric constant variation reported in Table 3.2.

Once the first objective, i.e. "to design a highly transmitting 3D printable meta-atom that can be used to control phase of the propagating field" was completed, the next aim was to "design phase manipulating surfaces by periodic arrangement of these meta-atoms". Metasurfaces can be designed by spatial periodic arrangement of proposed 3D printable meta-atoms in 2D orientation. These surfaces promise to offer the same transmission characteristics with relatively smaller height, so they can be used for near-field phase transformation. Smaller height means less use of material, enabling the surfaces to be low-cost compared to traditional all dielectric ones. Moreover as discussed in section 2.4, 3D printing is a simple and fast fabrication technique, and consequently fabrication of these surfaces will save time as well.

3.8 Chapter Summary

A detailed methodology to design metal-dielectric meta-atoms has been discussed and is then used to obtain full 2π phase gradient with high transmission magnitude (>-0.75 dB). Trends related to sensitivity of cell have been discussed and three parameters were identified affecting the phase shift and transmission magnitude of the cell. Phase manipulation was achieved by solving a large set of optimetrics comprising three parameters. The proposed unit cell is superior to all dielectric cell because the former achieved full phase gradient with less height. Low-profile, simple configuration and full phase gradient makes the cell highly suitable for various beam-forming applications.

Chapter 4

Beam Steering Metasurfaces

4.1 Introduction

This chapter explains the design of near-field phase manipulating metasurfaces. As an example, beam-steering metasurfaces have been designed and discussed. The metasurface has been designed using highly transmitting meta-atoms discussed in the previous chapter. Therefore, the surface has an extremely low reflection co-efficient. Proposed 3D printable non-planar surfaces have fine steering resolution and they are inexpensive compared to traditional methods [50].

This chapter is organized as follows, Section 4.2 explains the theory of phased array antennas, which forms the basis of beam-steering metasurfaces. The concept of phase wrapping has a great significance for beam-steering metasurfaces and is briefly explained in Section 4.3. Proposed metasurfaces, using meta-atoms, transform the electric near-field phase so that the beam is pointed in the desired direction. Conceptual design details of surfaces is explained in Section 4.4. Results predicted from simulations have shown that using the proposed metasurfaces, the beam can be relocated in any direction $\pm 40°$ with peak directivity of 24.5 dBi. A detailed discussion of the results is provided in Section 4.5. Finally, Section 4.6 concludes the chapter with the summary of the main points covered.

4.2 Phased Array Theory

An antenna array consists of spatially arranged antenna elements with each element having its own connector and input phase delay circuit [51]. Direction of the array beam is varied by feeding individual elements with distinct phase values. These phased array antennas do not require large mechanical structures for beam steering, and offer a fast steering solution. In a typical phased array antenna, several antenna elements are arranged in a 1D or 2D lattice. Increase in number of radiating elements adds to aperture size which enhances the directivity of the array. Figure 4.1 shows the schematic arrangement of an arbitrarily arranged 1D array with inter-element spacing *d*. The phased array theory states that the beam can be steered at an angle 'θ_o' away from the broadside. This can be done by introducing a progressive phase shift $\Delta\varphi$ between array elements, which is given as:

$$\Delta\varphi = kd\,sin(\theta) \tag{4.1}$$

Where k is wave number given by $2\pi/\lambda_o$ and θ is the desired tilt angle

$$\Delta\varphi = \frac{2\pi}{\lambda} \times d \times sin(\theta) \tag{4.2}$$

To obtain a broadside beam at θ_o=0° or 0° elevation angle, $\Delta\varphi$=0°

The aforementioned linear array yields a narrow fan beam with the narrow beamwidth in the plane of the array. To attain a pencil beam, the 1D array is extended into a 2D plane [52]. In the 1D or 2D array, grating lobes often appear if the inter-element spacing between array elements is greater than $\lambda_o/2$. They can be avoided by introducing proper inter-element spacing given as.

$$d_{max} = \frac{\lambda_o}{1+Sin(\theta)} \tag{4.1}$$

Where d_{max} is maximum allowable spacing between adjacent elements to avoid grating lobes. To steer beam at 30°, d_{max} is 0.66×lambda, while for 60° it is 0.54 ×lambda. In order to steer the beam by positive θ_o, in the 1D array illustrated in Figure 4.1, delay modules are adjusted such that the phase delay increases linearly from right to left. This results in changing the direction of radiation from broadside to an offset angle.

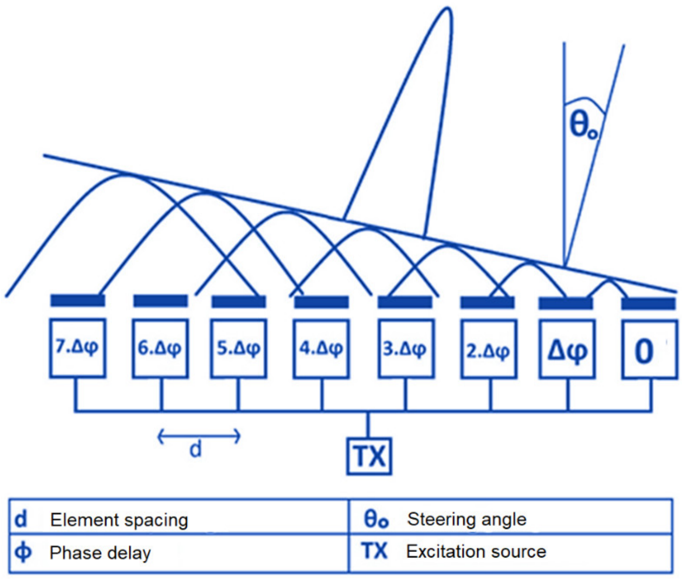

Figure 4.1: Phased array beam steering schematic setup.

To explain the process, let us consider an example of array setup operating at a frequency of 10 GHz (λ_o=30 mm), where the distance between radiating elements is 10 mm (λ_o/3). To steer the beam at 30° or θ_o=30°, the required progressive phase delay calculated is 60° or $\Delta\varphi$=60°. This mean that the incremental phase delay of radiating elements (in Figure 4.1) from right to left will be 0°, 60°, 120°, 180°, 240°, 300° and 360°. Because of periodicity of sinusoidal function used in equation (4.2), phase shift of 360° corresponds to 0° and the same sequence can be repeated for the rest of the array. This concept is referred to as phase wrapping, which is briefly explained in the following section.

4.3 Phase Wrapped and Un-wrapped Surfaces

As explained above, the absolute phase delay within the array increases along a linear axis to create the required gradient. The absolute phase delay within an array can be presented in two ways. If the phase delay in an array increases linearly with a constant slope, as shown in Figure 4.2(a), this is referred to as an unwrapped phase. It is understood that a periodic sinusoidal signal repeats after a phase of 2π or 360° or $\varphi_o = \varphi_o + 2n\pi$, where n is an integer. Hence, the absolute phase delay can be wrapped to 0° whenever it crosses value of 2π as shown in Figure 4.2(b), which is referred to as a wrapped phase. The phase wrapping is useful for phased array antennas and will be employed for metasurface design discussed in following sections. The phase wrapping explained for 1D array can be extended for a 2D array depicted by colour map plots in Figure 4.2. The figure shows two arbitrary size 2D arrays where antenna elements are represented by coloured square boxes. The colour in each box indicates the phase of the individual element. As can be seen in the figure, the phase increases linearly along one of the linear axes (x-axis here) and is constant along the orthogonal axis (y-axis here).

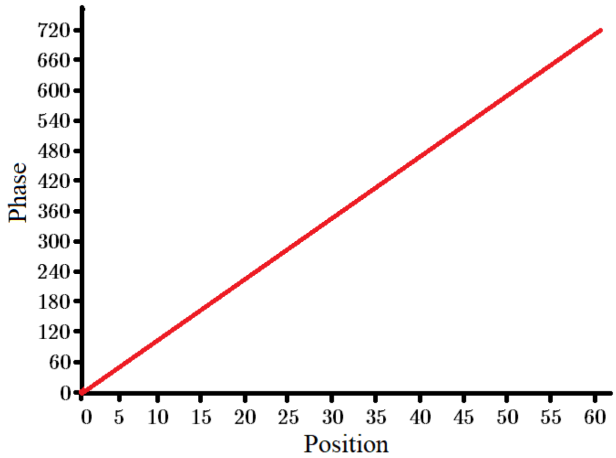

(a)

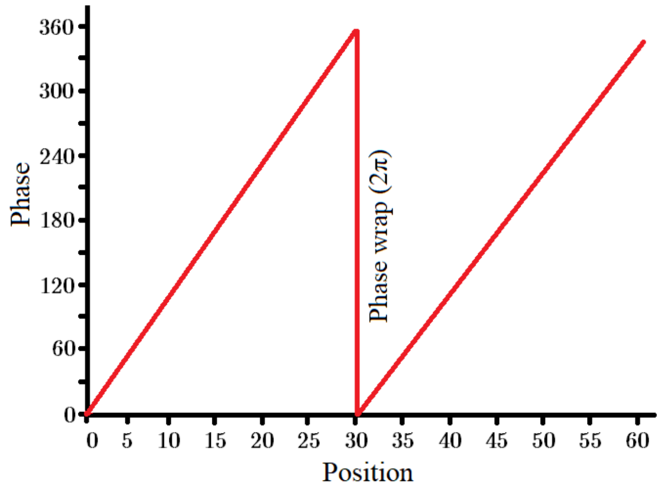

(b)

Figure 4.2: Linearly increasing phase-delay distributions for 1D array (a) un-wrapped and (b) wrapped distribution.

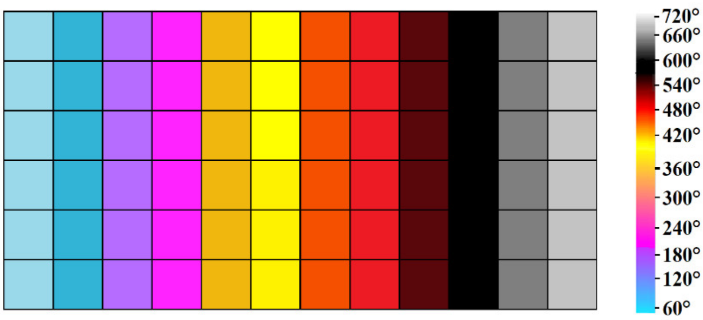

(a)

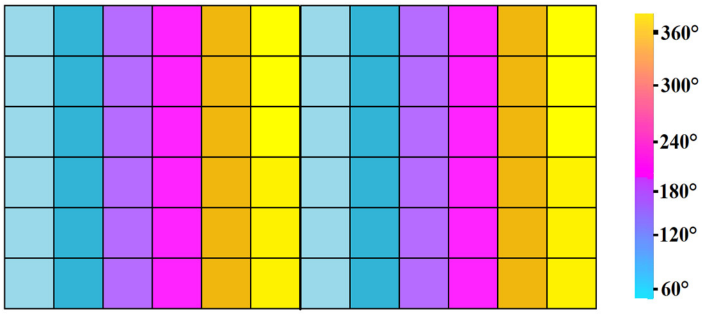

(b)

Figure 4.3: Phase delay in a 2D array (a) unwrapped (b) wrapped.

4.4 Metasurface Design

Using knowledge of array theory and phase wrapping, a metasurface can be designed (similar to 2D array), with spatial arrangement of meta-atoms, to create incremental phase shift in the x-axis (left to right), whereas a constant phase shift will be exhibited in the y-axis. It means identical meta-atoms will be required in the y-axis and meta-atoms with increasing phase shifts are needed to be arranged in the x-axis. Such a surface when used with antenna having uniform aperture phase distribution and beam in the broadside, simply turns its beam at an angle 'θ_o' away from the broadside.

To demonstrate the concept, a few metasurfaces are designed at the operating frequency of 20 GHz. All these metasurfaces have a lateral size of 90mm × 90mm (or $6\lambda_o \times 6\lambda_o$) and are made of 3D printable three layer meta-atoms discussed in Chapter 3. The first metasurface tilts the beam by 20° or $\theta_o=20°$. Using the array theory and treating the meta-atom of the surface as antenna elements of a 2D array, the relative phase shift can be obtained from equation (4.2). For the first metasurface: $\theta_o=20°$, d=25 mm (local periodicity of meta-atom) and $\lambda_o=15$ mm were used to calculate $\Delta\varphi$ in equation (4.2), which is ≃40° (or $\Delta\varphi \simeq 40°$).

Using $\Delta\varphi$, a 2D phase map is created for the metasurface. The phase increases along the x-axis of the metasurface starting from 40°. It is to be mentioned here that the starting value of the phase is not important, however, the phase gradient within metasurface is important.

This 2D map has nine distinct phase values: 40°, 80°... 360°, which are documented in Table 4.1. The tenth element must have a phase delay of 400°, which was wrapped back to 40° making it similar to the first element. The phase map is then used to select appropriate meta-atoms from the database of the three-layered meta-atoms discussed in Section 3.6. The physical characteristics of nine distinct meta-atoms are summarized in Table 4.1. The 2D metasurface with an aperture of 90mm × 90mm has 18x18 meta-atoms. The perspective view of the metasurface is shown in Figure 4.4(a).

In the figure, yellow square boxes on top of each dielectric block represent metallic patches. The patches are visible on the top side of the metasurface only, and an identical patch exists on the bottom side as highlighted in Figure 4.4(b). Height variation within the metasurface due the use of different meta-atoms is shown in Figure 4.4(b). This metasurface, in contrast to the reported planar metasurface, has a non-planar profile and permittivity variation which has never been investigated previously.

Table 4.1: Required phase value for tilt of 20° with corresponding dimensions of unit cell and transmission magnitude

Phase (degree)	**Dielectric constant (ε_r)**	**Height (mm)**	**Patch size (mm)**	**Magnitude (dB)**
40°	1.7	4.2	1.7	-0.0089
80°	3.5	3.3	1.7	-0.0149
120°	6.2	3.3	0.5	-0.4373
160°	3.5	7.2	1.7	-0.0662
200°	5.0	6.6	0.9	-0.0002
240°	6.6	3.6	3.5	-0.3156
280°	7.3	3.4	3.5	-0.2759
320°	7.8	7.1	1.9	-0.6220
360° (0°)	7.4	7.3	2.2	-0.3566
400° (40°)	1.7	4.2	1.7	-0.0089

A detailed study of phased array arrangement showed that arrangement in the x-axis was responsible for steering the beam to a particular angle, whereas the number of repetitions in the y-axis accounted for 3.0 dB bandwidth and sharpness of the lobe. Moreover the metasurface size and number of unit cells has also to do with directivity and achieved gain.

The second metasurface was designed for a tilt angle of 25°. In this case, phi increment of ~51.4385° or ($\Delta\varphi \simeq 51.4385°$) is required. Similarly to tilt beam to 30°, phi increment of 60° (or $\Delta\varphi \simeq 60°$) is required. To rotate beam to 25° required phase values with corresponding dimensions of three layer meta-atoms are mentioned in Table 4.2.

Table 4.2: Required phase value for tilt of 25° with corresponding dimensions of unit cell and transmission magnitude

Phase (degree)	Dielectric constant (ε_r)	Height (mm)	Patch size (mm)	Magnitude (dB)
51.4285°	1.7	6.9	0.9	-0.1572
102.857°	5.3	3.3	0.9	-0.0750
154.2855°	3.8	6.9	1.3	-0.3811
205.714°	5.0	4.8	2.9	-0.1027
257.1425°	7.1	3.3	3.9	-0.4697
308.571°	6.5	7.7	2.1	-0.3743
360° (0°)	7.4	7.3	2.2	-0.3566

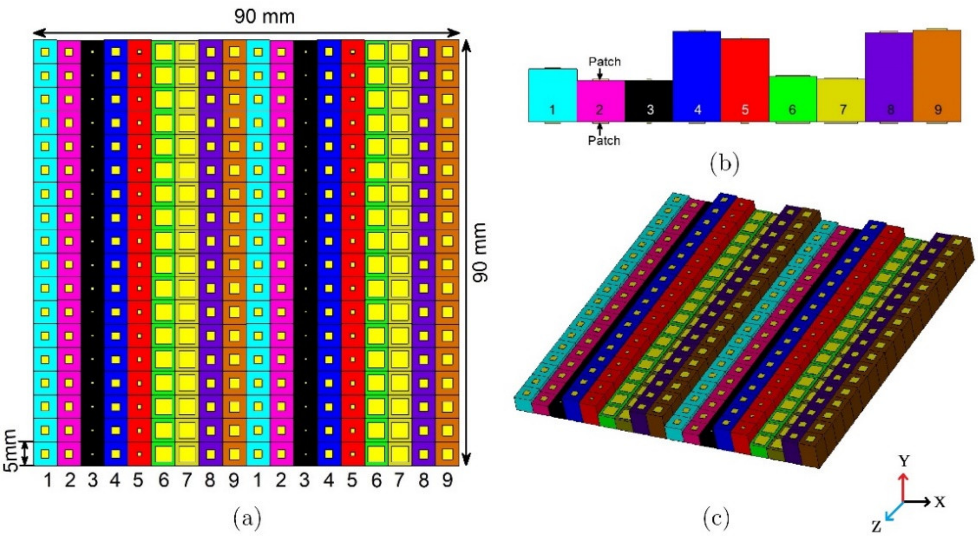

Figure 4.4: 2D metasurface with spatial arrangement of 9 elements designed to provide resultant θ_o=20° (a) top view (b) side view and (c) 3D view.

4.5 Results of Beam Steering

To validate the working of metasurfaces, they were simulated with a plane wave source. It was necessary to simulate metasurfaces with a plane wave because they were designed with the assumption of operating with an antenna that has uniform aperture phase distribution. Seven different metasurfaces were simulated for steering angles of 10°, 15°, 20°, 25°, 30°, 35° and 40°. Far-field results verified the beam tilting. Elevation cuts of the far-field pattern containing beam peaks are shown in Figure 4.5. Peak directivity of 24.5 dBi was achieved when tilt angle was at its minimum, i.e. 10°. From Figure 4.5 it can be observed that with the increase in value of tilt angle, directivity value begins to drop and dominance of side lobes tends to improve. For tilt angle of 10° side lobes are at their minimum, i.e. -10.35 dB and directivity is highest, whereas for 40° directivity is minimum and side lobes are at their highest value of -5.4 dB. After angle of 40° side lobes overtake the main lobe so this configuration is valid for angles up to 40°. Peak directivity value for tilt angle of 40° is 21.55 dBi.

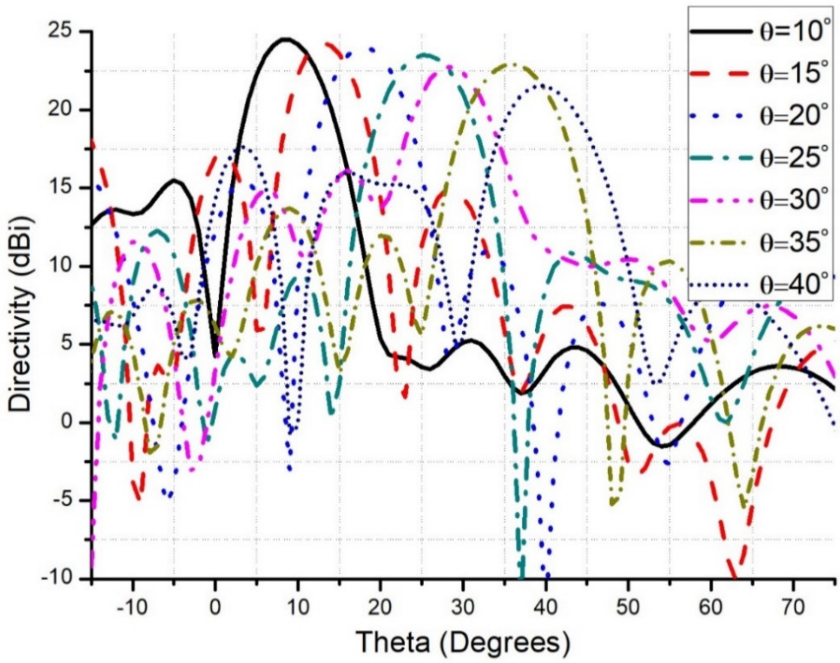

Figure 4.5: Beam steering results for various tilt angles versus directivity achieved for tilt angles ranging from 10° to 40°.

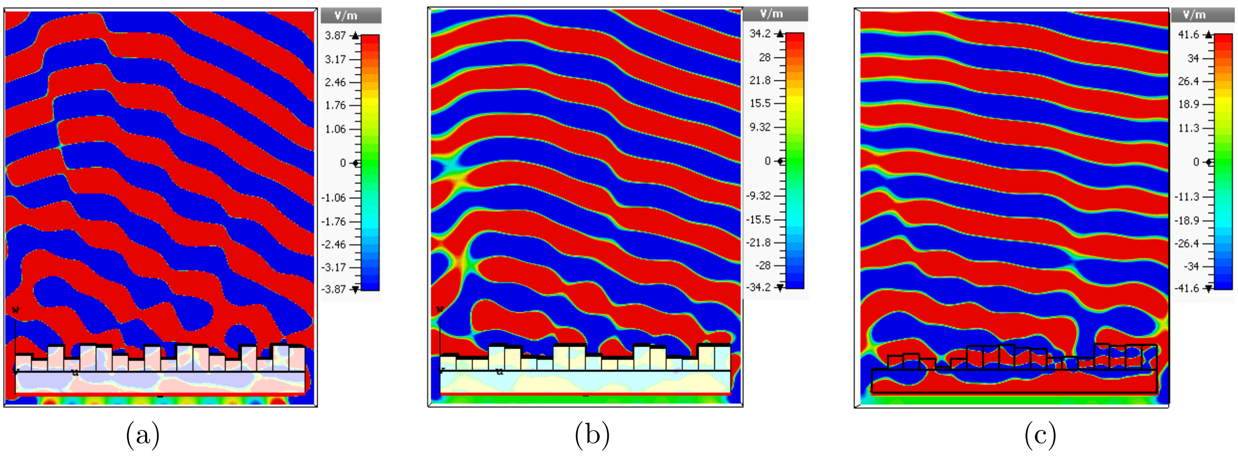

Figure 4.6: Near-field result for tilt angles of (a) 30°, (b) 20° and (c) 10°.

Beam tilting can also be observed from field propagation in the near-field scenario. Figure 4.6 shows electric field propagation out of three metasurfaces. As stated in section 4.4, metasurfaces have a finite size of $6\lambda_o \times 6\lambda_o$, which indicates that surfaces have been designed for finite plane and scan angle. Aperture truncation error was expected for near-field simulations because of finite scan area (scan plane truncation) [53]. It can be seen in Figure 4.6 that for all three cases, a section of the wave towards extreme right deviates from the desired tilt angle. This is because of truncation of aperture size and it can be reduced using various mathematical techniques like Gerchberg-Papoulis Algorithm and integral equation technique. However, that issue is beyond the scope of this dissertation [53], [54].

4.6 Chapter Summary

A detailed methodology to design highly transmitting 3D printable phase manipulating surfaces by periodic arrangement of metal-dielectric meta-atoms has been discussed. Design of metasurfaces is based on phased array arrangement theory which does not require additional mechanism for operation. Simulation results of beam steering have been presented for 7 different tilt angles. Peak directivity of 24.5 dBi was achieved when the surface was designed for a tilt angle of 10° and plane wave was designated as excitation source.

Chapter 5

Medium-Gain Beam Steering Antenna

This chapter presents a design example of a beam steering antenna using the 3D printable metasurface discussed in Chapter 4. Metasurfaces have been designed to steer the beam of an RCA, which is low-profile, highly directive and functions as a simple feed antenna. Results predicted by simulations have shown that a maximum gain of 21.65 dBi was achieved with side lobe levels (SLL) of -14.44 dB. Using different metasurfaces, the RCA beam has been steered at various elevation angles.

5.1 Resonant Cavity Antenna (RCA)

To demonstrate the designed surface's application, it was placed in the near-field of classical RCA to manoeuvre its response to the anticipated angle. The antenna system was designed to operate at the frequency of 20 GHz. The RCA comprises a microstrip patch antenna, and a partially reflecting surface (PRS). The patch is printed on the Rogers UltraLam2000 slab (t_1 = 1.57 mm, ε_{r1} = 2.5) dielectric substrate while the PRS (partially reflecting surface) is made up of Rogers TMM10 (t_2 = 1.24 mm, ε_{r2} = 9.2) dielectric slab, pictorially shown in Figure 5.1(a). Length of PRS in the x-y plane is 90 mm ($6\lambda_o$) each. The spacing between the ground plane and the PRS is $\lambda_o/2$ (7.5 mm at the operating frequency). Classical RCAs with less reflective PRSs are known to have shortcoming of non-uniform electric near-field phase distribution [55]. This is because the proposed metasurface assumes a uniform phase or time-delay distribution of electric fields at the input and cannot operate properly with these RCAs. Therefore, a non-planar metal-dielectric permittivity gradient phase correcting surface (PG-PCS) is introduced to create a uniformity in phase distribution of RCA.

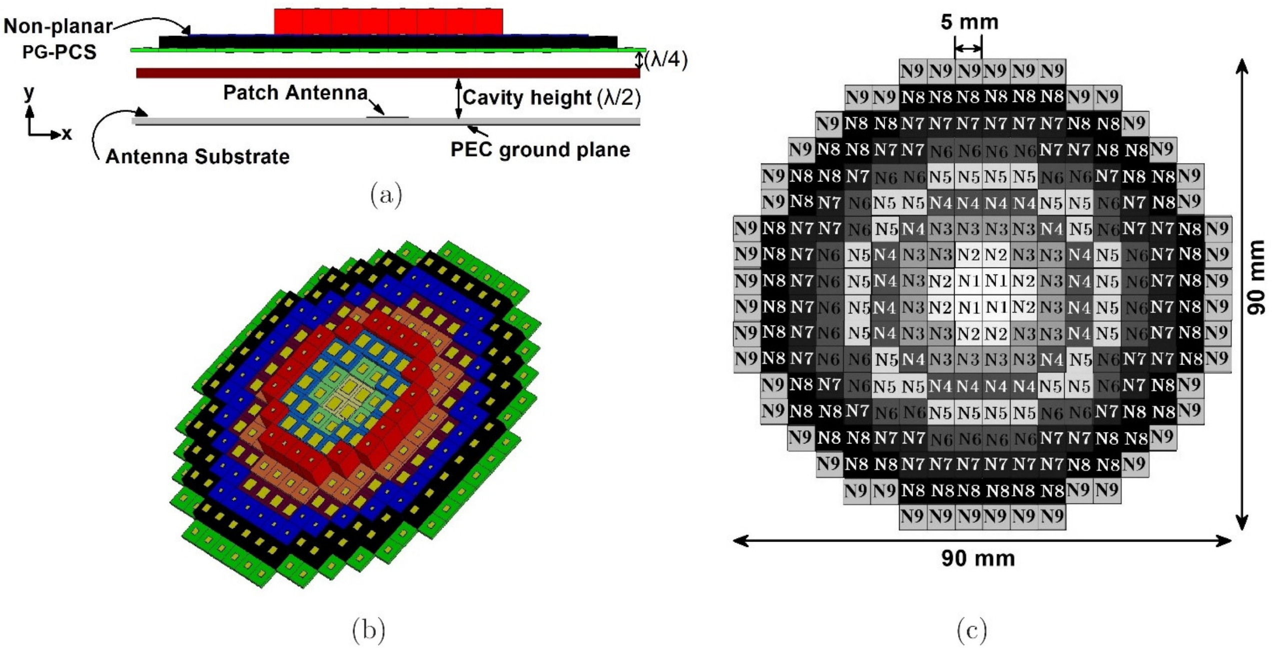

Figure 5.1: Phase correcting setup for RCA (a) PG-PCS with antenna (b) 3D view of PCS (c) grayscale plot of circular symmetry of phase distribution on which PG-PCS will be placed.

5.2 PG-PCS Design for RCA

PG-PCS design methodology is similar to that described in [43].Since RCA is known to have rotationally symmetric aperture phase distribution, the phase is probed on the aperture and phase correction required from the PG-PCS is calculated. Following the approach similar to that of beam steering metasurfaces, the required phase correction used to select appropriate meta-atoms forms PG-PCS. It is pertinent to mention here that the design of PG-PCS is not main objective of this thesis, however, its performance differs from traditional PCS (phase correcting surfaces) for the following reasons.

1. All cells used in PG-PCS are highly transmitting so it has a very low reflection coefficient. Correcting surface only alters the phase of the input signal and does not diminish its amplitude, which in turn provides higher gain compared to traditional PCS [43], [46].
2. It is non-planar as well as permittivity gradient which means both permittivity and height were varied simultaneously in the design process. Therefore it is 70% smaller in height compared to the PCSs presented in the literature [43], [46].

PG-PCS was placed at a distance of $\lambda_o/4$ (3.75 mm) above the PRS, as shown in Fig 5.2. It converted the RCA's spherical wavefront to a relatively planar wavefront. Apart from this the surface also increased the antenna's directivity by 7.0 dBi and increased aperture efficiency by 23.8%. Table 5.1 shows dielectric constant, height and patch values for corresponding sections of PG-PCS shown in Figure 5.1(c).

Table 5.1: Dielectric blocks dielectric constant, height and patch size for various sections of PG-PCS marked from N1 to N9 in Figure 5.1(c).

S. No.	PG-PCS section	Dielectric constant (ε_r)	Height (mm)	Patch (mm)
1	N1	5.3	4.5	3.1
2	N2	5.6	5.1	2.3
3	N3	3.2	6.0	3.1
4	N4	3.2	7.5	0.9
5	N5	5.0	3.0	1.7
6	N6	2.9	2.4	2.7
7	N7	3.8	3.0	0.9
8	N8	2.0	2.7	1.9
9	N9	1.1	0.6	1.5

5.3 RCA Beam Steering

Once planar response with improved gain was achieved for RCA, beam steering metasurfaces were placed at the height $\lambda_o/4$ (3.75 mm) above PG-PCS. Figure 5.2 displays the complete configuration of the setup with base antenna, PG-PCS and beam steering metasurface. Figure 5.3 shows gain for various tilt angles. RCA beam was steered to different angles depending on the metasurfaces' respectively designed tilt angles. The maximum gain achieved was 21.65 dBi for the scenario when the metasurface had tilt angle of 10° concerning the antenna**.** The RCA beam peak was scanned to the maximum angle of 35°. The peak gain value varied with the metasurfaces but variation was not more than 2.0 dBi.

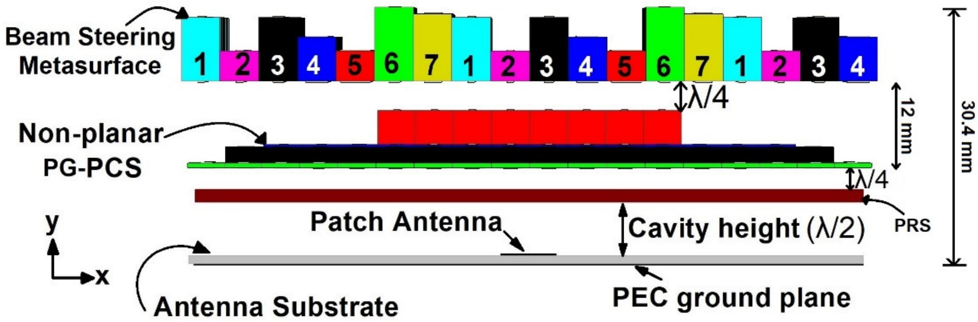

Figure 5.2: Beam steering antenna system. PG-PCS will convert spherical response of antenna to relatively planar profile and metasurface will steer the planar response to desired direction.

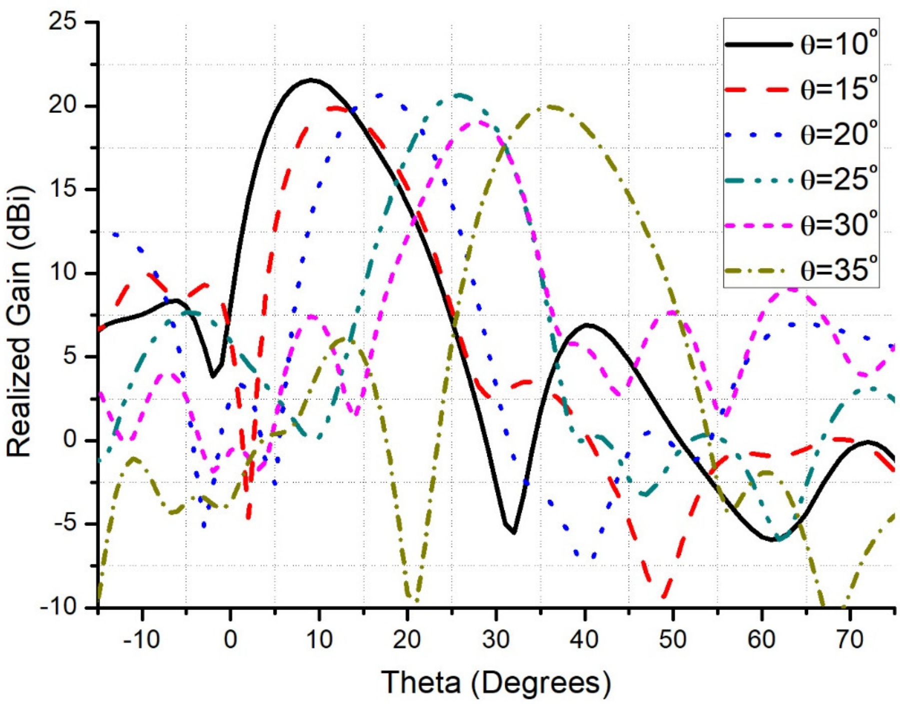

Figure 5.3: Far-field elevation cuts of the RCA with PG-PCS and different metasurfaces for tilt angles of 10°, 15°, 20°, 25°, 30° and 35°.

Chapter 6

Conclusion and Future work

This research focused on designing 3D printable metal-dielectric metasurface for beam steering using a phased array arrangement. The important findings from this investigation are described in this chapter, which also outlines the recommended directions for future research.

6.1 Conclusions

Low cost 3D printable meta-atoms have been proposed, which can offer complete phase shift of 360° with insertion loss >-0.75 dB. Metasurface designed using meta-atoms has 40% less height compared to all dielectric surface. The maximum dielectric constant value of material is 8.0 which helps to avoid commercial materials with high dielectric constant which are comparatively expensive. The 3D printing process is used because it can manufacture materials of arbitrary height and dielectric constant which are commercially not available. Using proposed patch mounted unit cell configuration, artificial materials of desired permittivity can be manufactured. As an application, phased array metasurfaces are developed and are placed in the near-field region of a RCA. Each metasurface tilts the radiation beam at an offset angle away from the broadside direction. Patterns degrade when the beam is pointed farthest from the broadside. However, the peak gain in all cases remains within 2 dB limit of the highest gain of 21.65 dBi. Research showed that a very low-profile beam steering antenna system can be designed using the near-field phase delay metasurfaces. It is possible to achieve beam steering without having to physically move the feeding antenna, which here is RCA. A totally passive beam steering system can be realized. Presence of active components/devices is avoided because they increase design complexity, cost, and losses.

6.2 Future Work

This research work reveals scope for further investigation of metasurfaces composed of artificial dielectrics. The possibilities are as follows:

- Simple 3D printable meta-atom configuration has been explored in this work but other complex cell shapes can be tried as long as they provide full phase range control. Various cell configurations have been explored in the optical domain and can be implemented for beam-forming applications in the EM domain [56], [57].
- Proposed metasurfaces are highly transmitting because they have minimum transmission magnitude (S21) of -0.75 dB. This value can be reduced further by exploring the factors that influence transmission characteristics of meta-atoms. Wider dielectric constant range will further reduce reflection coefficient. Also it will help to reduce dielectric height because we will be able to achieve complete phase shift with less height.
- This study concluded that gain and pattern quality of the antenna degrade when the beam moves further away from the broadside. The gain and quality of the pattern can be improved by simplifying and optimizing the metasurface design. Various optimization techniques can be employed, for instance particle swarm optimization (PSO) and generic algorithm (GA) [58], [59].
- Proposed metasurfaces can be tested to alter responses of other EM components such as microstrip antennas and horn antennas.

Appendices

Appendix A

Incident electric field on interface can be expressed as

$$E_i = E_{i0}e^{-jk_1z} \tag{A.1}$$

Here E_{i0} represents incident E-field, k_1 is wave number in dielectric media and z denotes the direction of propagation. By Maxwell equations,

As $\eta = \frac{E_0}{H_o}$, so incident, reflected and transmitted fields can be expressed as.

$$H_i = H_{i0}e^{-jk_1z} = \frac{E_{i0}}{\eta_1}e^{-jk_1z}$$

$$E_r = E_{r0}e^{jk_1z} \tag{A.2}$$

$$H_r = -H_{r0}e^{jk_1z} = -\frac{E_{r0}}{\eta_1}e^{-jk_1z}$$

$$E_t = E_{t0}e^{-jk_2z} \tag{A.3}$$

$$H_t = H_{t0}e^{-jk_2z} = \frac{E_{t0}}{\eta_2}e^{-jk_2z}$$

Using the boundary conditions at z=0 the tangential components of the electric and magnetic fields in both regions are equal:

$$E_i + E_r = E_t \tag{A.4}$$

$$H_i + H_r = H_t$$

$$\frac{E_i}{\eta_1} - \frac{E_r}{\eta_1} = \frac{E_t}{\eta_2} \tag{A.5}$$

Substitute (A.4) in (A.5) to get

$$\frac{E_i}{\eta_1} - \frac{E_r}{\eta_1} = \frac{E_i + E_r}{\eta_2}$$

$$\frac{E_i}{\eta_1} - \frac{E_r}{\eta_1} = \frac{E_i}{\eta_2} + \frac{E_r}{\eta_2}$$

$$\frac{E_i}{\eta_1} - \frac{E_i}{\eta_2} = \frac{E_r}{\eta_1} + \frac{E_r}{\eta_2}$$

$$E_i\left[\frac{\eta_2 - \eta_1}{\eta_1\eta_2}\right] = E_r\left[\frac{\eta_2 + \eta_1}{\eta_1\eta_2}\right]$$

$$\frac{E_r}{E_i} = \frac{\eta_2 - \eta_1}{\eta_2 + \eta_1} = \Gamma = Reflection\ Coefficient$$

Similarly, the solution for $\frac{E_t}{E_i}$ yields

$$\frac{E_t}{E_i} = \frac{2\eta_2}{\eta_2 + \eta_1} = T = Transmission\ Coefficient$$

Where Γ and T are used here to represent the reflection and transmission coefficients at the interface, respectively. Since the reflecting surface is planar and the incident field is linearly polarized, the transmitted and reflected fields will also be linearly polarized. Because the direction of polarization of transmitted and reflected electric fields is unknown, they are assumed here to be in the same direction (positive) as the incident electric fields. If that is not the case, it will be corrected by the appropriate signs on the reflection and transmission coefficients.

For more complex scenarios, where multiple reflections through media are taken in consideration, we can calculate the transmission and reflection coefficients using matrices [47], [60].

$$\begin{bmatrix} E_{1+} \\ E_{1-} \end{bmatrix} = \frac{1}{\tau_1}\begin{bmatrix} 1 & \rho_1 \\ \rho_1 & 1 \end{bmatrix}\begin{bmatrix} E'_{1+} \\ E'_{1-} \end{bmatrix} = \frac{1}{\tau_1}\begin{bmatrix} 1 & \rho_1 \\ \rho_1 & 1 \end{bmatrix}\begin{bmatrix} e^{jk_1l_1} & 0 \\ 0 & e^{-jk_1l_1} \end{bmatrix}\begin{bmatrix} E_{2+} \\ E_{2-} \end{bmatrix}$$

$$\frac{1}{\tau_1}\begin{bmatrix} 1 & \rho_1 \\ \rho_1 & 1 \end{bmatrix}\begin{bmatrix} e^{jk_1l_1} & 0 \\ 0 & e^{-jk_1l_1} \end{bmatrix}\frac{1}{\tau_2}\begin{bmatrix} 1 & \rho_2 \\ \rho_2 & 1 \end{bmatrix}\begin{bmatrix} E'_{2+} \\ 0 \end{bmatrix}$$

We assume that E'_{2-}=0, so

$$E_{1+} = \frac{e^{jk_1l_1}}{\tau_1\tau_2}(1 + \rho_1\rho_2e^{-2jk_1l_1})E'_{2+}$$

$$E_{1-} = \frac{e^{jk_1l_1}}{\tau_1\tau_2}(\rho_1 + \rho_2e^{-2jk_1l_1})E'_{2+}$$

This can be solved for reflection and transmission responses

$$\Gamma_1 = \frac{E_{1-}}{E_{1+}} = \frac{\rho_1+\rho_2e^{-2jk_1l_1}}{1+\rho_1\rho_2e^{-2jk_1l_1}} \tag{A.6}$$

$$T = \frac{E'_{2+}}{E_{1+}} = \frac{\tau_1\tau_2e^{-jk_1l_1}}{1+\rho_1\rho_2e^{-2jk_1l_1}} \tag{A.7}$$

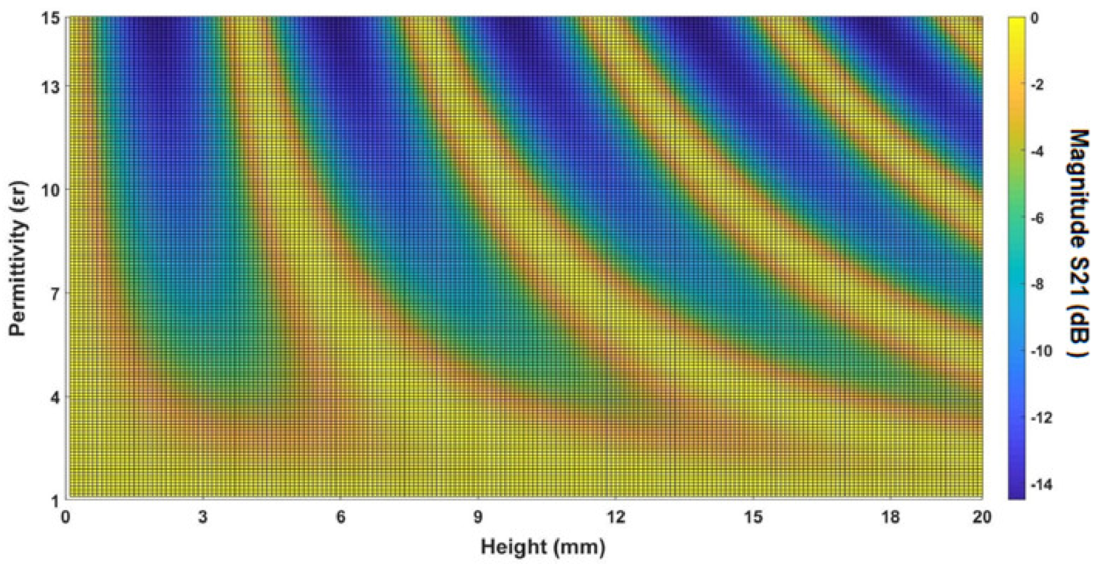

(a)

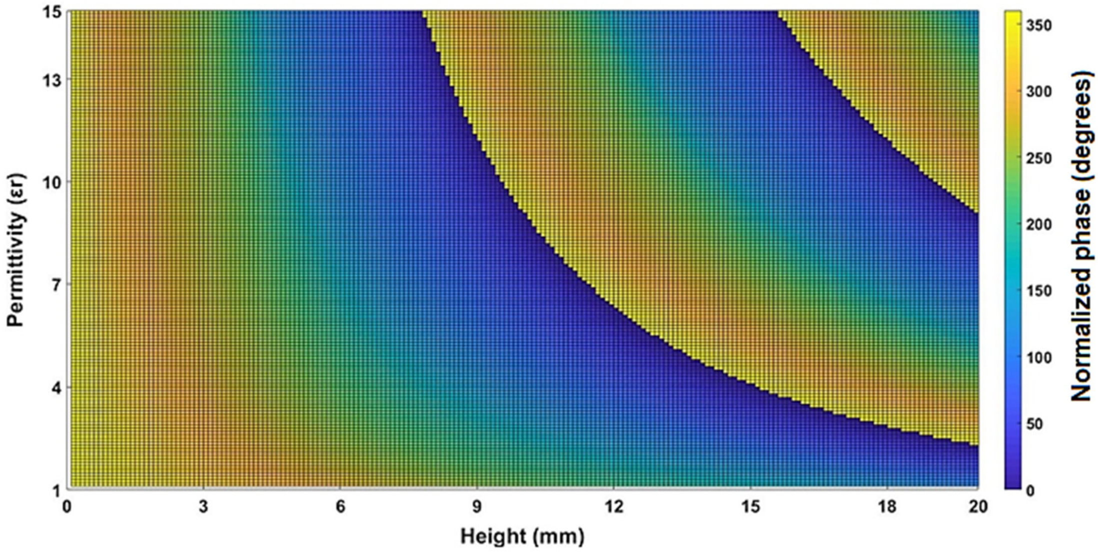

(b)

Figure A.1: Transmission coefficient in the thickness vs dielectric constant space for a frequency of 20 GHz; (a) with colour bar of magnitude (in dB), (b) with colour bar of normalized wrapped phase (in degrees).

Equation (A.7) can be plotted to retrieve information pertaining to transmission characteristics of dielectrics, where thickness and dielectric constant of material are significant parameters that account for insertion loss and phase shift of the bare sample (dielectric without patch). These parameters must be carefully chosen so that transmission is high**.** Plots of transmission magnitude versus dielectric constant and phase versus dielectric constant are shown in Figures A.1(a) and A.1(b) respectively. These surface plots help us to select a range of parameters to achieve full phase gradient with low insertion loss. From Figure A.1 we infer that the dielectric slab with larger height seemingly has the potential to obtain greater phase shift range while maintaining a high transmission coefficient. However, large thickness is not recommended because the cell becomes bulky, heavy and since more material is required, more expensive. Consequently, a compromise must be reached.

The thinner the structure, the more attractive it is in terms of weight and material cost. However, if the structure is too thin, it will be difficult to obtain a good phase shift range. Similarly, the dielectric constant of the structure must be wisely selected. A low dielectric constant will not lead to a broad phase shift range while a high dielectric constant will lead to a small practical phase shift range due to the low transmission coefficient. After some preliminary studies, the dielectric constant range was selected from 1.1 to 8.0 and the thickness between 1.0 mm and 14.0 mm. The reason for doing is that this range makes it possible to achieve 360° phase shift with extremely low insertion loss. Figure A.2 illustrates simulated transmission results for all dielectric unit cells with full phase shift of 2π.

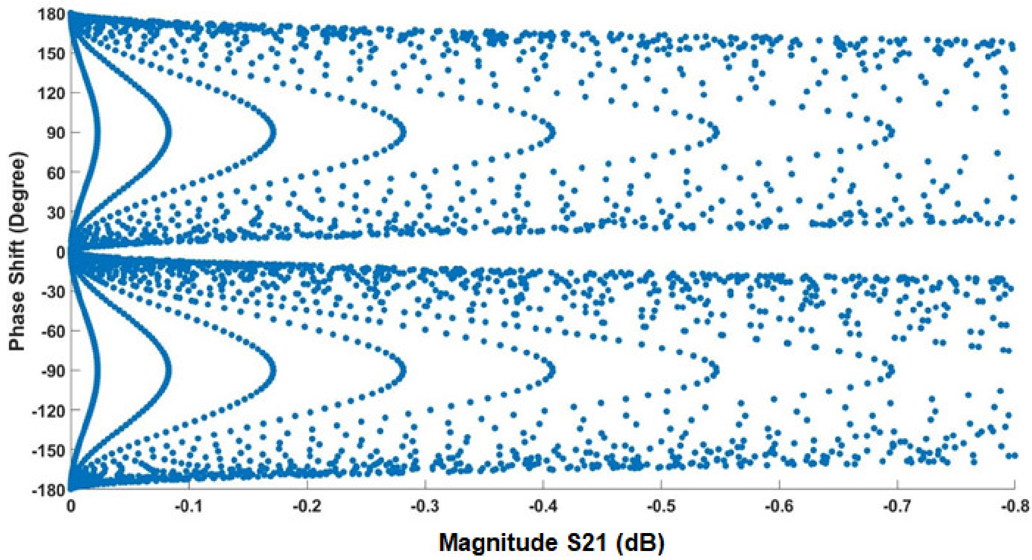

Figure A.2: Simulated transmission results for all dielectric unit cells for dielectric constant variation ranging from 1.1 to 8.0, and where height varies from 0.5mm to 14mm.

Appendix B

List of Acronyms

ABS	Acrylonitrile Butadiene Styrene
AM	Additive Manufacturing
AMF	Additive Manufacturing File
CAD	Computer-Aided Design
CAGR	Compound Annual Growth Rate
EM	Electromagnetic
FDM	Fused Deposition Modelling
FSS	Frequency Selective Surfaces
GA	Generic Algorithm
GRIN	Graded-Index
HFSS	High Frequency Structure Simulation
LED	Light Emitting Diode
PASS	Phase and amplitude shifting structures
PCS	Phase Correcting Structure
PG-PCS	Permittivity gradient phase correcting structure
PLA	Polylactic acid
PRS	Partially reflecting structure
PS	Phase Shifting
PSO	Particle Swarm Optimization
RCA	Resonant Cavity Antenna
RF	Radio Frequency
SLL	Side Lobe Levels

References

[1] “Reflector for use in wireless telegraphy and telephony,” U.S. Patent No. 1301473 Feb. 1919.

[2] H. Lamb, “On the Reflection and Transmission of Electric Waves by a Metallic Grating,” *Proc. London Math. Soc.*, vol. s1-29, no. 1, pp. 523–546, Nov. 1897.

[3] G. Zheng, H. Mühlenbernd, M. Kenney, G. Li, T. Zentgraf, and S. Zhang, “Metasurface holograms reaching 80% efficiency,” *Nat. Nanotechnol.*, vol. 10, no. 4, pp. 308–312, May 2015.

[4] Q. Wang *et al.*, “Broadband metasurface holograms: toward complete phase and amplitude engineering,” *Sci. Rep.*, vol. 6, no. 1, p. 32867, Dec. 2016.

[5] L. Li *et al.*, “Electromagnetic reprogrammable coding-metasurface holograms,” *Nat. Commun.*, vol. 8, no. 1, p. 197, Dec. 2017.

[6] Y. Guo, X. Hou, X. Lv, K. Bi, M. Lei, and J. Zhou, “Tunable artificial microwave blackbodies based on metasurfaces,” *Opt. Express*, vol. 25, no. 21, p. 25879, Oct. 2017.

[7] N. (Nader) Engheta, R. W. Ziolkowski, and Institute of Electrical and Electronics Engineers., *Metamaterials : physics and engineering explorations.* Wiley-Interscience, 2006.

[8] F. Liu, S. Xiao, A. Sihvola, and J. Li, “Perfect Co-Circular Polarization Reflector: A Class of Reciprocal Perfect Conductors With Total Co-Circular Polarization Reflection,” *IEEE Trans. Antennas Propag.*, vol. 62, no. 12, pp. 6274–6281, Dec. 2014.

[9] Y. Ra’di, V. S. Asadchy, and S. A. Tretyakov, “Total Absorption of Electromagnetic Waves in Ultimately Thin Layers,” *IEEE Trans. Antennas Propag.*, vol. 61, no. 9, pp. 4606–4614, Sep. 2013.

[10] N. Yu and F. Capasso, “Flat optics with designer metasurfaces,” *Nat. Mater.*, vol. 13, no. 2, pp. 139–150, Feb. 2014.

[11] “Polarization-Independent and Ultrawideband Metamaterial Absorber Using a Hexagonal Artificial Impedance Surface and a Resistor-Capacitor Layer,” *IEEE Trans. Antennas Propag.*, vol. 62, no. 5, pp. 2652–2658, May 2014.

[12] X. Chen, T. M. Grzegorczyk, B.-I. Wu, J. Pacheco, and J. A. Kong, “Robust method to

retrieve the constitutive effective parameters of metamaterials," *Phys. Rev. E*, vol. 70, no. 1, (Pt. 2) p. 016608, Jul. 2004.

[13] S. Zhang, W. Whittow, and J. (Yiannis) C. Vardaxoglou, "Additively manufactured artificial materials with metallic meta-atoms," *IET Microwaves, Antennas Propag.*, vol. 11, no. 14, pp. 1955–1961, Nov. 2017.

[14] J. Brown and J. S. Seeley, "The fields associated with an interface between free space and an artificial dielectric," *Proc. IEEE Part C Monogr.*, vol. 105, no. 8, pp. 465-471, 1958.

[15] J. Machac, "Microstrip line on an artificial dielectric substrate," *IEEE Microw. Wirel. Components Lett.*, vol. 16, no. 7, pp. 416–418, Jul. 2006.

[16] A. Brown, "Correction to "Pattern Shaping with a Metal Plate Lens"," *IEEE Trans. Antennas Propag.*, vol. 29, no. 3, pp. 550–550, May 1981.

[17] I. Bahl and P. Bhartia, "Leaky-wave antennas using artificial dielectrics at millimiter wave frequencies," in *1980 Antennas and Propagation Society International Symposium*, vol. 18, pp. 23–26.

[18] A. L. Garner, G. J. Parker, and D. L. Simone, "Predicting effective permittivity of composites containing conductive inclusions at microwave frequencies," *AIP Adv.*, vol. 2, no. 3, p. 032109, Sep. 2012.

[19] W. E. Kock, "Metallic Delay Lenses," *Bell Syst. Tech. J.*, vol. 27, no. 1, pp. 58–82, Jan. 1948.

[20] W. Rotman, "Plasma simulation by artificial dielectrics and parallel-plate media," *IRE Trans. Antennas Propag.*, vol. 10, no. 1, pp. 82–95, Jan. 1962.

[21] K. Golden, "Plasma simulation with an artificial dielectric in a horn geometry," *IEEE Trans. Antennas Propag.*, vol. 13, no. 4, pp. 587–594, Jul. 1965.

[22] J. Stangel, "The thinned lens approach to phased array design," in *1965 Antennas and Propagation Society International Symposium*, vol. 3, pp. 10–13.

[23] R. A. Silin, "optical properties of dielectrics (review)," *Radiophys. Quantum Electron.,* vol. 15, no. 6, pp. 615-624, June 1962.

[24] V. K. Valev *et al.*, "Nonlinear Superchiral Meta-Surfaces: Tuning Chirality and Disentangling Non-Reciprocity at the Nanoscale," *Adv. Mater.*, vol. 26, no. 24, pp. 4074–4081, Jun. 2014.

[25] Y. Zhu, X. Hu, Z. Chai, H. Yang, and Q. Gong, "Active control of chirality in nonlinear metamaterials," *Appl. Phys. Lett.*, vol. 106, no. 9, p. 091109, Mar. 2015.

[26] K. Song, X. Zhao, Y. Liu, Q. Fu, and C. Luo, "A frequency-tunable 90°-polarization rotation device using composite chiral metamaterials," *Appl. Phys. Lett.*, vol. 103, no. 10, p. 101908, Sep. 2013.

[27] N. Gagnon, A. Petosa, and D. A. McNamara, "Thin microwave phase-shifting surface lens antenna made of square elements," *Electron. Lett.*, vol. 46, no. 5, pp. 327-329, 2010.

[28] Y. Li, M. F. Iskander, Z. Zhang, and Z. Feng, "A New Low Cost Leaky Wave Coplanar

Waveguide Continuous Transverse Stub Antenna Array Using Metamaterial-Based Phase Shifters for Beam Steering," *IEEE Trans. Antennas Propag.*, vol. 61, no. 7, pp. 3511–3518, Jul. 2013.

[29] H. Markovich, D. Filonov, I. Shishkin, and P. Ginzburg, "Bifocal Fresnel Lens Based on the Polarization-Sensitive Metasurface," *IEEE Trans. Antennas Propag.*, vol. 66, no. 5, pp. 2650–2654, May 2018.

[30] V. R. Gowda, M. F. Imani, T. Sleasman, O. Yurduseven, and D. R. Smith, "Focusing Microwaves in the Fresnel Zone With a Cavity-Backed Holographic Metasurface," *IEEE Access*, vol. 6, pp. 12815–12824, 2018.

[31] A. D. Khan and M. Amin, "Polarization Selective Multiple Fano Resonances in Coupled T-Shaped Metasurface," *IEEE Photonics Technol. Lett.*, vol. 29, no. 19, pp. 1611–1614, Oct. 2017.

[32] A. Perigaud, S. Bila, O. Tantot, N. Delhote, and S. Verdeyme, "3D printing of microwave passive components by different additive manufacturing technologies," in *2016 IEEE MTT-S International Microwave Workshop Series on Advanced Materials and Processes for RF and THz Applications (IMWS-AMP)*, 2016, pp. 1–4.

[33] M. Dressler, T. Studnitzky, and B. Kieback, "Additive manufacturing using 3D screen printing," in *2017 International Conference on Electromagnetics in Advanced Applications (ICEAA)*, 2017, pp. 476–478.

[34] "Le marché de l'impression 3D pourrait être de 8,41 milliards de dollars en 2020 - MonUnivers3D." [Online]. Available: http://www.monunivers3d.com/2278/. [Accessed: 22-May-2018].

[35] S. Zhang, W. Whittow, and J. (Yiannis) C. Vardaxoglou, "Additively manufactured artificial materials with metallic meta-atoms," *IET Microwaves, Antennas Propag.*, vol. 11, no. 14, pp. 1955–1961, Nov. 2017.

[36] S. Zhang, R. K. Arya, S. Pandey, Y. Vardaxoglou, W. Whittow, and R. Mittra, "3D-printed planar graded index lenses," *IET Microwaves, Antennas Propag.*, vol. 10, no. 13, pp. 1411–1419, Oct. 2016.

[37] J. Fell, "3D printing takes off [for aerospace manufacturing]," *Eng. Technol.*, vol. 11, no. 10, pp. 72–75, Nov. 2016.

[38] M. Rizwan, M. W. A. Khan, H. He, J. Virkki, L. Sydänheimo, and L. Ukkonen, "Flexible and stretchable 3D printed passive UHF RFID tag," *Electron. Lett.*, Jun. 2017.

[39] J. R. McGhee, M. Sinclair, D. J. Southee, and K. G. U. Wijayantha, "Strain sensing characteristics of 3D-printed conductive plastics," *Electron. Lett.*, vol. 54, no. 9, pp. 570–572, May 2018.

[40] "3D Printing Materials Market Global Trends 2017 to 2024, Future Growth & Industry Drivers - openPR." [Online]. Available: https://www.openpr.com/news/627932/3D-Printing-Materials-Market-Global-Trends-2017-to-2024-Future-Growth-Industry-Drivers.html.

[Accessed: 22-May-2018].

[41] "3ders.org - 3D Hubs adds 1,000 new printers and releases their 3D Printing Trends Report for June 2015 | 3D Printer News & 3D Printing News." [Online]. Available: https://www.3ders.org/articles/20150603-3d-hubs-adds-3d-printers-releases-their-3d-printing-trends-report-for-june-2015.html. [Accessed: 22-May-2018].

[42] B. Biernacki, S. Zhang, and W. Whittow, "3D printed substrates with graded dielectric properties and their application to patch antennas," in *2016 Loughborough Antennas & Propagation Conference (LAPC)*, 2016, pp. 1–5.

[43] M. U. Afzal, K. P. Esselle, and B. A. Zeb, "Dielectric Phase-Correcting Structures for Electromagnetic Band Gap Resonator Antennas," *IEEE Trans. Antennas Propag.*, vol. 63, no. 8, pp. 3390–3399, Aug. 2015.

[44] R. K. Arya, S. Pandey, and R. Mittra, "Flat lens design using artificially engineered materials," *Prog. Electromagn. Res. C*, vol. 64, pp. 71–78, 2016.

[45] M. U. Afzal, K. P. Esselle, and A. Biswas, "A method to enhance radiation characteristics by improving aperture phase distribution of electromagnetic bandgap resonators antennas," in *2015 International Conference on Electromagnetics in Advanced Applications (ICEAA)*, 2015, pp. 561–564.

[46] M. U. Afzal and K. P. Esselle, "A Low-Profile Printed Planar Phase Correcting Surface to Improve Directive Radiation Characteristics of Electromagnetic Band Gap Resonator Antennas," *IEEE Trans. Antennas Propag.*, vol. 64, no. 1, pp. 276–280, Jan. 2016.

[47] S. J. Orfanidi, "Reflection and Transmission," in Electromagnetic Waves and Antennas. Piscataway, NJ, USA: Rutgers University, 2011, pp. 154–185.

[48] R. Mittra and Y. Zhou, "A new look at the transformation electromagnetics approach for some real-world applications," *Philos Trans A Math Phys Eng Sci.*, vol. 373 (2049), Aug. 2015.

[49] R. K. Arya, S. Pandey, and R. Mittra, "Flat Lens Design Using Artificially Engineered Materials," *Prog. Electromagn. Res. C*, vol. 64, pp. 71–78, 2016.

[50] I. Uchendu and J. R. Kelly, "Survey of beam steering techniques available for millimeter wave applications," *Prog. Electromagn. Res. B*, vol. 68, pp. 35–54, 2016.

[51] E. Topak, J. Hasch, C. Wagner, and T. Zwick, "A Novel Millimeter-Wave Dual-Fed Phased Array for Beam Steering," *IEEE Trans. Microw. Theory Tech.*, vol. 61, no. 8, pp. 3140–3147, Aug. 2013.

[52] Mailloux, Robert J. "Phased Array Antenna Handbook Second Edition," vol. 2. Boston: Artech house, 2005.

[53] E. Martini, O. Breinbjerg, and S. Maci, "Reduction of Truncation Errors in Planar Near-Field Aperture Antenna Measurements Using the Gerchberg-Papoulis Algorithm," *IEEE Trans. Antennas Propag.*, vol. 56, no. 11, pp. 3485–3493, Nov. 2008.

[54] F. J. Cano-Fácila, S. Pivnenko, and M. Sierra-Castañer, "Reduction of Truncation Errors in Planar, Cylindrical, and Partial Spherical Near-Field Antenna Measurements," *Int. J. Antennas Propag.*, vol. 2012, pp. 1–19, Feb. 2012.

[55] Y. Li *et al.*, "Directivity enhancement of fabry-perot antenna by using a stepped-dielectric slab superstrate," *Microw. Opt. Technol. Lett.*, vol. 54, no. 3, pp. 711–715, Mar. 2012.

[56] H.-X. Xu *et al.*, "Tunable microwave metasurfaces for high-performance operations: dispersion compensation and dynamical switch," *Sci. Rep.*, vol. 6, no. 1, p. 38255, Dec. 2016.

[57] C. Liu *et al.*, "Fully Controllable Pancharatnam-Berry Metasurface Array with High Conversion Efficiency and Broad Bandwidth," *Sci. Rep.*, vol. 6, no. 1, p. 34819, Dec. 2016.

[58] A. Lalbakhsh, M. U. Afzal, and K. P. Esselle, "Multiobjective Particle Swarm Optimization to Design a Time-Delay Equalizer Metasurface for an Electromagnetic Band-Gap Resonator Antenna," *IEEE Antennas Wirel. Propag. Lett.*, vol. 16, pp. 912–915, 2017.

[59] J. Robinson and Y. Rahmat-Samii, "Particle Swarm Optimization in Electromagnetics," *IEEE Trans. Antennas Propag.*, vol. 52, no. 2, pp. 397–407, Feb. 2004.

[60] C. A. Balanis, *Advanced Engineering Electromagnetics.* Wiley, 1989.